

Table 9.1: Electron vacancy number of alloying elements.⁽⁹⁾

$N_v^i \dots$	Al ...	7.66
	Ti, Si ...	6.66
	Cr, Mo, W ...	4.66
	Mn ...	3.66
	Fe ...	2.66
	Co ...	1.71
	Ni ...	0.66

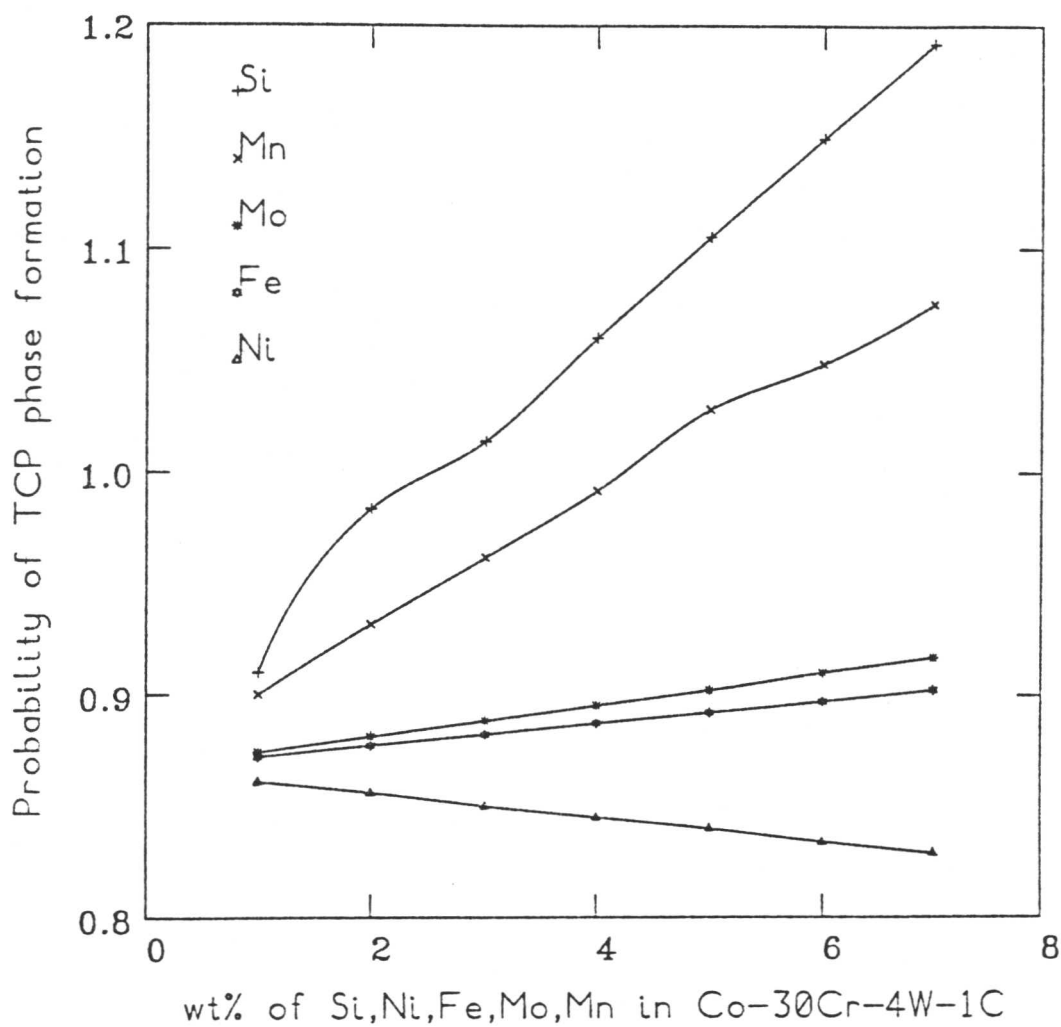


Fig. 9.3 Effect of alloying elements Si, Mn, Mo, Fe and Ni on the probability of TCP phase formation in Co-30Cr-4W-1.0C (wt%) alloy.

9.6 Conclusions

In a microstructure consisting of a mixture of carbides in a soft matrix, it is approximately the case that the hard carbide particles provide the resistance to abrasion whereas the tough matrix serves the role of binding the relatively brittle carbides. Both the matrix and carbide phases have to contain sufficient chromium to make the alloy corrosion and oxidation resistant. Since the matrix phase loses its strength more rapidly with an increase in temperature, it has to be solid solution strengthened for elevated temperature service (hence the tungsten addition).

The size of the carbide particles becomes particularly important when compared with the width of wear grooves created by abrasion. If the size is comparable to the width of the grooves, then experiments suggest that the carbides may be removed completely into the chips which are created as a consequence of the micromachining processes associated with groove formation. It has also been reported that when the matrix-carbide interface is relatively weak, the detachment of fine carbides can leave behind a pitted surface with poor wear resistance. An advantage of closely-spaced (presumably finer) carbides may be that they strengthen the matrix, thereby reducing its rate of erosion by abrasive particles; however, this can only be significant at very small particle sizes and it is probably better to strengthen the matrix by other mechanisms such as solid solution alloying, which do not entail an undue reduction in carbide particle size. Relatively coarse carbides have to be damaged extensively before they substantially enter the wear debris. These factors are important since any carbides introduced into the debris can themselves act as abrasives and enhance the wear rate.

When abrasive particles are much harder than the carbide, the large carbides can undergo considerable deep cutting, spalling and cracking; in these circumstances, the carbide particle size should not be excessively large compared with groove width, and the toughness of the carbide becomes important.

During low-stress abrasion, an increase in the volume fraction of carbides (from 0.3 to 0.5) leads to a corresponding increase in the macroscopic hardness of the alloy and in the wear resistance. This relationship must have a maximum, perhaps corresponding to a point where there is a loss of contiguity in the matrix phase, but this issue does not seem to have been investigated. During gouging (i.e., aggressive abrasion), the wear rate initially decreases with the volume fraction of carbides, but subsequently begins to increase due to the fracture, spalling and pull-out of carbide particles.

The critical role of the tough-matrix in supporting the carbides, and the fact that the matrix has to be reasonably resistant to abrasion has been emphasised in many studies. Unlike the carbides, the matrix is able to undergo considerable plastic deformation prior to fracture. Consequently, it is the hardness of the *work hardened* surface which correlates with improved wear resistance. For cobalt-based Stellite alloys, the matrix is face-centered cubic in crystal structure, but its thermodynamically stable form is hexagonal close-packed (hcp). The fcc→hcp transformation can occur by faulting on every second plane in a stack of close-packed planes.

Consequently, the stacking fault energy of the fcc matrix is relatively low, $10\text{-}50\text{ mJm}^{-2}$, giving rise to partial dislocations and a high work hardening rate. Alloying elements which reduce the stacking fault energy increase the work hardening rate and the resistance to heavy abrasion (galling) and erosion; however, low-stress abrasion wear resistance, which depends more on the total carbide content, is not greatly influenced by stacking fault energy.

The addition of alloying elements alters the thermodynamic stability of the fcc and hcp phases by either enlarging or constricting their fields. Among the alloying elements, Mn, Ni and Fe have a strong effect on the SFE, stabilizing the fcc allotrope, on the other hand Mo, W and Cr stabilize the hcp phase and decrease the SFE.

The stability range of the intermetallic compounds in Co-based hardfacing alloys varies as a function of chemical composition. Si and Mn are the most effective alloying elements in stabilising these compounds.

Finally, a refinement in the scale of microstructure is known to have beneficial effects on the abrasive wear resistance and mechanical properties, although the earlier reservations about too fine a carbide size must be borne in mind.

9.7 References

- 1) K. C. ANTONY: *J. of Metals*, Feb., 1983, **35**, 52.
- 2) *Metals Handbook*, 9th edn, 1983, 771, ASM, USA.
- 3) J. L. DE BROUWER, and D. COUTSOURADIS: *COBALT*, 1966, **32**, 141.
- 4) T. C. TISONE: *Acta Metall.*, 1973, **21**, 229.
- 5) T. ERICSSON: *Acta Metall.*, 1966, **14**, 853.
- 6) D. M. BUCKLEY: *Cobalt*, 1968, **38**, 20.
- 7) W. M. STEEN: *Metals and Materials*, 1985, **1**, (12), 736.
- 8) T. H. KOSEL, and N. F. FIORE: *J. Materials for Energy Systems*, 1981, **3**, 7.
- 9) V. M. DESAI, C. M. RAO, T. H. KOSEL, and N. F. FIORE: *Wear*, 1984, **94**, 89.
- 10) H. R. SHETTY, T. H. KOSEL, and N. F. FIORE: *Wear*, 1982, **80**, 347.
- 11) J. D. B. DE MELLO, M. DURANDE-CHARRE, and T. MATHIA: *Wear*, 1986, **111**, 203.
- 12) H. R. SHETTY, T. H. KOSEL, and N. F. FIORE: in Proc. Conf. 'Wear of Materials 1981', 1981, New York, 379.
- 13) T. H. KOSEL, N. F. FIORE, J. P. COYLE, S. P. UDVARDY, and W. A. KONKEL: in Proc. Conf. 'Corrosion-Erosion Behavior of Materials', St. Louis, Missouri, October 1978, Metallurgical Society of AIME, 190.
- 14) L. V. MUYSEN: *Cobalt*, 1972, **55**, 67.
- 15) W. SILENCE: in Proc. Conf. 'Wear of Materials 77', St. Louis, April 1977, Am. Soc. Mech. Eng., 77.
- 16) D. N. NOBLE: 'The effect of flux-cored arc welding conditions on microstructure and abrasive wear resistance of two iron-based hardfacing alloys', Report 7856.02/86/479.3, Welding Institute Res. Report, November 1986.
- 17) A. M. EL-RAKAYBY, and B. MILLS: *Wear*, 1986, **112**, 327.
- 18) K. H. ZUM GAHR: *Z. Metallkde.*, 1980, **71**, 103.
- 19) R. C. D. RICHARDSON: *Wear*, 1967, **10**, 291.
- 20) J. LARSEN-BADSE: *Trans. of the Metall. Soc. of AIME*, 1966, **236**, 1461.
- 21) R. W. K. HONEYCOMBE: 'Steels, Microstructure and Properties', 1981, 22.
- 22) L. REMY: *Metall. Trans. A*, 1981, **12A**, 387.
- 23) B. ROEBUCK, E. A. ALMOND, and A. M. COTTENDEN: *Materials Science and Engineering*, 1984, **66**, 179.
- 24) L. REMY, and A. PINEAU: *Materials Science and Engineering*, 1976, **26**, 123.
- 25) K. J. BHANSALI, and A. E. MILLER: *Wear*, 1982, **75**, 241.
- 26) P. CROOK, and C. C. LI: in Proc. Conf. 'Wear of Materials 83', New York, 1983, Am. Soc. Mech. Eng., 298.
- 27) C. J. HEATHCOCH, A. BALL, and B. E. PROTHEROE: *Wear*, 1981-1982, **74**, 11.

- 28) J. SUGITANI, and M. TAKAHASHI: Kubota Tech. Rep., 1982, **7**, (1), 14.
- 29) Y. KONDO, K. YASUE, M. ISOTANI, and K. SHIMADA: Rep. Gov. Ind. Res. Inst. Nagoya, 1980, **29**, (12), 362.
- 30) J. MAZUMDER, C. CUSANO, A. GHOSH, and C. EIHOLZER: in Proc. Conf. 'Laser Processing of Materials', AIME, 1984, 199.
- 31) E. A. METZBOWER, E. R. PIERPOINT, and K. HARTMANN: in the "Changing Frontiers of Laser Material Processing", in Proc. Conf. "5th International Conference in Application of Lasers and Electro Optics, 1986.
- 32) J. SINGH, and S. RANGANATHAN: Phy. Stat. Sol., 1981, **73**, 243.
- 33) W. BOLLMANN: Acta Metall., 1961, **9**, 972.
- 34) C. HITZENBERGER, H. KARNTHALER, and A. KORNER:
- 35) Z. BASINSKI, and J. W. CHRISTIAN: Phil. Mag., 1953, **44**, 791.
- 36) S. MAHAJAN, M. GREEN, and D. BRASEN: Metall. Trans. A, 1977, **8A**, 283.
- 37) H. FUJITA, and S. UEDA: Acta Metall., 1972, **20**, 759.
- 38) K. RAJAN: Metall. Trans. A, 1982, **13A**, 1161.
- 39) "Superalloys II", Eds. T. S. CHESTER, S. S. NORMAN, C. H. WILLIAM, New York, 1987.

10. COMPARISON OF THE MICROSTRUCTURES OF STELLITE HARDFACING ALLOYS DEPOSITED BY ARC WELDING AND LASER CLADDING

10.1 Introduction

Cobalt-based hardfacing alloys are used in applications requiring good wear, oxidation and corrosion properties during service at elevated temperatures.^(1,2) In their commercially available forms, they most commonly derive their hardness from the presence of a high volume fraction ($\approx 0.2-0.3$) of carbides and are referred to as *Stellites*. The cobalt-based hardfacing alloys are the most popular within the Stellite range; their typical composition is Co-28Cr-4W-1.1C wt.%, and they can be deposited by processes such as arc welding, laser cladding etc. The first phase to form during cooling from the liquid state consists of unfaceted cobalt-rich dendrites with a face-centered cubic (fcc) crystal structure. The remaining liquid eventually solidifies by a eutectic reaction into an interdendritic, intimate lamellar mixture of the fcc phase and $(\text{Cr, Co, W})_7\text{C}_3$ eutectic carbides. The carbide is chromium rich with a typical composition $(\text{Cr}_{0.85}\text{Co}_{0.14}\text{W}_{0.01})_7\text{C}_3$, depending on alloy composition and cooling conditions; it is henceforth referred to as M_7C_3 carbide.

The relationship between microstructure and wear properties can be confusing and is not well established; indeed, wear is not just a property of the hardfacing alloy, but also of the type of abrasive involved and of the specific wear process (impact, corrosion-erosion etc.).⁽³⁻⁶⁾ It is therefore emphasised at the outset that the microstructure is just a part of the wear problem. On the other hand, it is well established that the microstructure is an important component in determining the properties of hardfacing alloys, and since at least a working hypothesis is necessary in any alloy design procedure, the microstructure-wear relationship for cobalt-based alloys was reviewed in Chapter 9.

The specific purpose of this chapter is to examine any differences in microstructure between cobalt-based hardfacing alloys deposited by three different techniques: manual metal arc welding, tungsten inert gas welding and laser cladding. In Chapter 11 the microscopy of wear in the same alloys will be examined.

10.2 Experimental Methods

The experimental alloys were deposited using three different processes: manual metal arc (MMA) welding, tungsten inert gas (TIG) welding and laser cladding.

The MMA welds were deposited in three layers, on a base plate of 4cm thickness. The top layer could therefore be examined in an essentially undiluted condition. The welding was carried out using 4mm diameter electrodes, the deposition conditions being 160A, 23V (AC), with a welding speed of about 0.004ms^{-1} and an interpass temperature of about 350°C . The nominal

electrical energy input is therefore 920Jmm^{-1} . The compositions of the base plate and of the top layer are given in Table 10.1.

Each of the TIG and laser clad specimens was deposited in five layers in the form of five overlapping Stellite 6 tracks, each track overlapping a previous track by 20%, three of the tracks forming the first layer with the second layer consisting of the other two tracks. The laser operated at 4kW power and 5mm beam diameter, the deposit being shielded by helium. The workpiece speed was 0.5m/min, the wire being inclined at an angle of 45° into the leading edge of the beam. The 1.2mm diameter wire (Stellite 6, Table 10.1) was fed in at 1m/min.

TIG welding was carried out using a 2.4mm diameter 2% thoriated tungsten electrode, 10-12V DC (electrode -ve), 150A current, 5mm electrode stickout, 10mm diameter nozzle, a torch angle of 10° from the vertical and a rod angle of 10° from the horizontal. The nominal heat input is estimated to be about 660J/mm. The composition of the 3.2mm diameter Stellite 6 rod used is given in Table 10.1; an Argon shielding gas was used, the flow rate being $6.7 \times 10^{-5} \text{ m}^3\text{s}^{-1}$.

Note that the deposition conditions used for this work are typical for each of the three processes, the aim being to compare the processes in their current state of development. The thickness of the deposits obtained are 12, 3 and 2mm for the MMA, TIG and laser clad samples respectively.

Metallographic specimens, both cross-sections normal to the welding direction and longitudinal sections from the top layer were etched using a solution of 100ml water, 10ml nitric acid, 50ml HCl and 10g iron chloride. Vicker's hardness measurements were carried out on these samples using 5g and 95g loads. The backscattered imaging technique of scanning electron microscopy was used in order to observe any segregation of tungsten; highly polished and unetched samples were prepared for this purpose, in order to avoid topographic contrast.

Thin foil specimens for transmission electron microscopy were prepared from $\approx 1.5\text{mm}$ thick discs spark-machined from the TIG and laser clad deposits; for the MMA deposits, discs were cut from 3mm diameter rods machined from the top layer. They were subsequently thinned and electropolished in a twin-jet polishing unit using a 20% perchloric acid, 10% glycerol, and 70% ethyl alcohol at 0°C and 35 volts. The foils were examined using a Philips EM 400T transmission electron microscope operated at 120kV.

Microanalysis experiments were also carried out using this microscope, with an energy dispersive X-ray analysis facility. The specimens were held in a beryllium holder tilted 35°C from the normal, this angle being the take-off angle. The X-ray count rate was optimised at about 900 counts/s over a count period of 100s, giving a typical statistical accuracy of about 1%. The data were analysed using the LINK RTS-FLS program for thin foil microanalysis, this corrects the data for atomic number, and absorption, and accounts for overlapping peaks by fitting standard profiles. However, it should be noted that due to the strong absorption of the tungsten "M" line, and to avoid overlap with the Si K_{α} line, the tungsten "L" line was used during the analysis of the X-ray spectra. Even though the probe diameter used was about 3nm, beam

spreading due to the scattering of electrons within the thin foil gave an estimated broadened beam diameter of $\approx 20\text{nm}$. Since the interdendritic M_7C_3 carbides in the TIG and laser clad samples were of the order of 20nm in size, a scanning transmission electron microscopy mode was used during microanalysis, providing access to smaller spot sizes. It should be noted that the microanalytical system used cannot cope with light elements such as carbon, so that the results (Z_i) are quoted throughout as atomic percentages of the total substitutional alloy content.

Table 10.1: Chemical compositions (wt.%).

	MMA Base	MMA Deposit	TIG Base	TIG Wire	Laser Base	Laser Wire
C	0.094	1.19	0.16	1.39	0.17	1.37
Si	0.55	0.72	0.28	1.06	0.27	0.94
Mn	0.71	0.08	0.83	–	0.76	1.26
Ni	–	2.67	0.03	0.22	0.03	–
Cr	–	28.91	0.05	27.5	0.07	29.9
Mo	–	0.01	0.16	0.01	0.08	–
W	–	4.81	–	4.82	–	4.90
Co	–	58.53	–	62.24	–	57.33
Fe	98.65	3.08	98.49	2.76	98.62	4.30

A thin foil thickness correction was found necessary to account for atomic absorption. The thickness was in each case measured using the two beam convergent beam electron diffraction technique proposed by Kelly *et al.* ⁽⁷⁾ This method is capable of giving an accuracy of 2% or better and has the additional advantage that the thickness can be measured locally in the area of interest. This method is based on the equation derived from the two beam dynamical theory of electron diffraction. The equation yields;

$$(S_i / n_i)^2 + (1 / n_i)^2 (1 / \xi_g)^2 = 1 / t^2 \quad \dots (1)$$

where, ξ_g is the effective extinction distance, t is the specimen thickness, S_i is the deviation of the i th minimum from the exact Bragg position, and n_i is the integer.

S_i is given by;

$$S_i = \lambda / d^2 (L_i / L_0) \quad \dots (2)$$

where,

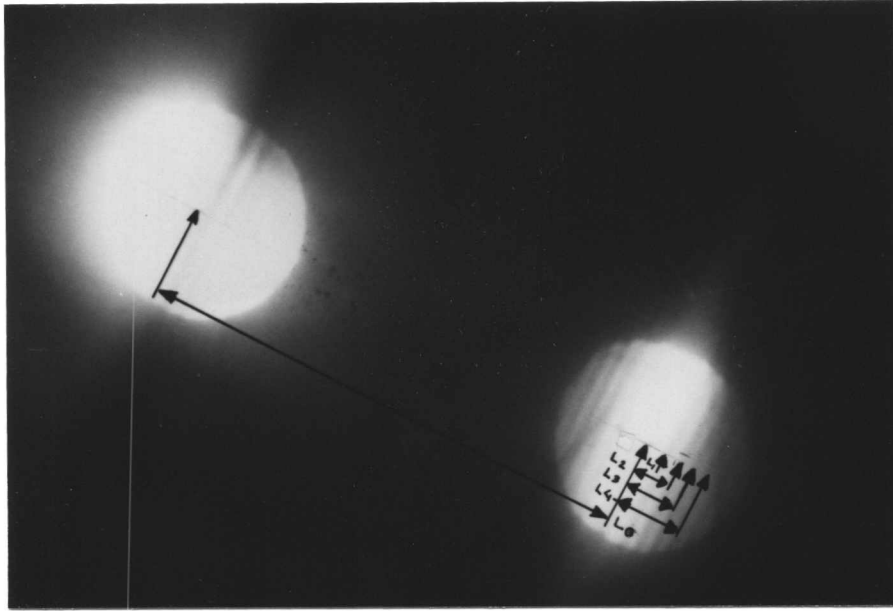
λ = wavelength of the incident beam,

d = spacing of the reflecting planes,

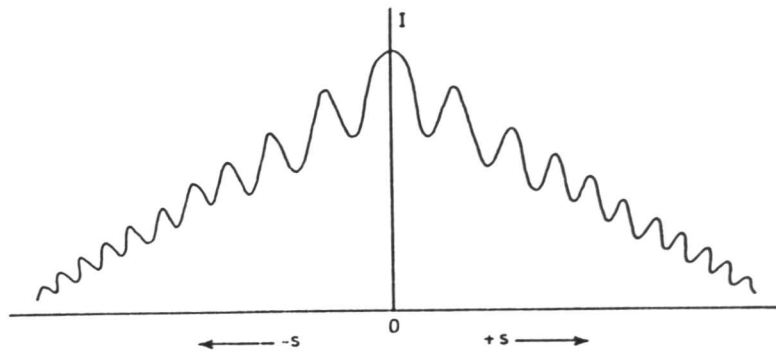
L_0 = distance from the centre of the diffracted beam profile to the centre of the transmitted beam,

L_1, L_2, \dots = distances from the centre of the diffracted beam profile to each of the successive minima.

Fig. 10.1 shows the two beam diffraction pattern and the distances explained above by using (113) reflection of the fcc matrix, and Table 10.2 gives (L_i / L_0) distances corresponding to S_i values. Plotting $(S_i / n_i)^2$ against $(1 / n_i)^2$ gives the thickness (or more strictly $1 / t^2$) as the intercept on the (S_i / n_i) axis. The slope of the straight line gives a value for the extinction distance ξ_g . It is necessary to establish the value of n_1 , i.e. the value for the first minimum. For a thin foil that is between $m\xi_g$ and $(m + 1)\xi_g$ thick the appropriate value of n_1 is $m + 1$, and the successive n_i values are $m + 2$, $m + 3$, etc. The choice of the correct value for n_1 can be obtained from a trial plot of $(S_i / n_i)^2$ versus $(1 / n_i)^2$. This will only give a straight line when the correct n_1 is selected. Table 10.3 gives the calculated $(S_i / n_i)^2$ and $(1 / n_i)^2$ values for $i = 1, 2, 3, 4$, and 5. The regression analyses were carried out using the data given in Table 10.3 and the best fit to a straight line (which is determined by the correlation coefficient, r) was observed for $n_1 = 3$, (Table 10.4) corresponding to a foil thickness of 1183 Å (Fig. 10.2).



a



b

Fig. 10.1: a) Magnified image of a two beam convergent beam diffraction pattern taken from the fcc Co-rich matrix; b) showing minima corresponding to the diffracted beam.

Table 10.2: Measured (L_i / L_0) and corresponding S_i values using the (113) fcc reflection of the fcc matrix.

i	L_i/L_0	λ	d	S_i
1	0.029			1.11×10^{-3}
2	0.0639			2.44×10^{-3}
3	0.093	0.03347 Å	1.0685 Å	3.55×10^{-3}
4	0.116			4.44×10^{-3}
5	0.145			5.55×10^{-3}

Table 10.3: $(S_i / n_i)^2$ and $(1 / n_i)^2$ values for $i = 1, 2, 3, 4, 5$, using the data given in Table 10.2.

		$i=1$	$i=2$	$i=3$	$i=4$	$i=5$
$n_i = 1$	$(1/n_i)^2$	1				
	$(S_i/n_i)^2$	1.236×10^{-6}				
$n_i = 2$		0.25	0.25			
		3.085×10^{-7}	1.493×10^{-6}			
$n_i = 3$		0.111	0.111	0.111		
		1.371×10^{-7}	6.636×10^{-7}	1.404×10^{-6}		
$n_i = 4$		0.0625	0.0625	0.0625	0.0625	
		7.713×10^{-8}	3.733×10^{-7}	7.898×10^{-7}	1.233×10^{-6}	
$n_i = 5$		0.04	0.04	0.04	0.04	0.04
		4.936×10^{-8}	2.389×10^{-7}	5.055×10^{-7}	7.896×10^{-7}	1.234×10^{-6}
$n_i = 6$			0.0277	0.0277	0.0277	0.0277
			1.659×10^{-7}	3.510×10^{-7}	5.483×10^{-7}	8.570×10^{-7}
$n_i = 7$				0.0204	0.0204	0.0204
				2.579×10^{-7}	4.0286×10^{-7}	6.296×10^{-7}
$n_i = 8$					0.01562	0.01562
					3.084×10^{-7}	4.821×10^{-7}
$n_i = 9$						0.01234
						3.809×10^{-7}

Table 10.4: Correlation coefficients (r) and t values corresponding to each n_i .

n_1	r	t (A)
1	0.212	864
2	0.9954	1043
3	0.9962	1183
4	0.9939	1304
5	0.9779	1412

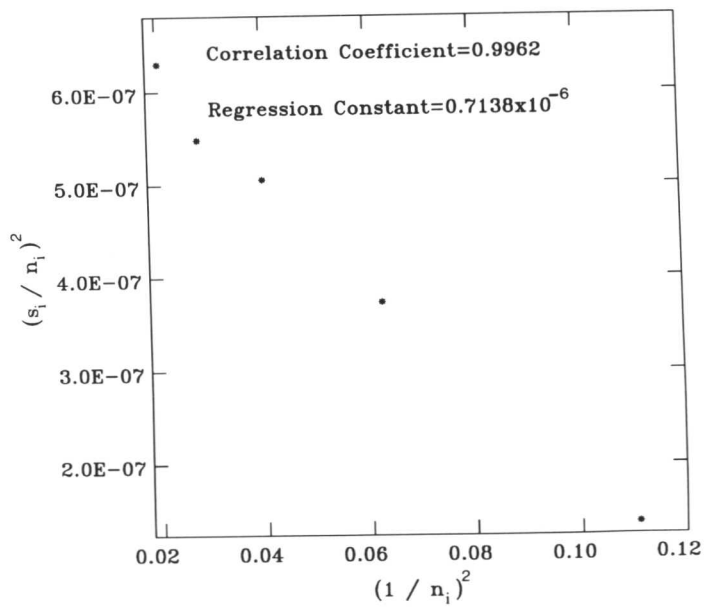


Fig. 10.2: Illustration of the plot of $(S_i / n_i)^2$ versus $(1 / n_i)^2$ for $N_1 = 3$.

The error bars quoted throughout the text, for the microanalysis results, are those from the *LINK* system and represent a conservative overestimate of the statistical error.

To follow distribution of the alloying elements over a larger scale, some microanalytical experiments were carried out using an energy dispersive X-ray analysis system on a scanning electron microscope. The data were corrected for atomic number, absorption, and fluorescence using the *LINK* software mentioned earlier.

10.3 Results and Discussion

10.3.1 Dilution

Since the base plates differ in composition from the hardfacing alloys, and since the former will to some extent melt during welding, the mixing of the resultant liquid with the hardfacing deposit leads to dilution effects.^(8,9) The effects of dilution are expected to be greatest in the vicinity of the base plate although the spread of dilution into the fusion zone must depend on process variables such as freezing rate, and turbulence and convective flows within the melt pool. As will be discussed later, dilution has important microstructural consequences. Experiments were carried out on a scanning electron microscope, to determine the chemical composition variation along the centerline, across the fusion boundary between the base plate and the first layer.

The results (Fig. 10.3) are significantly different for the three processes; the extent of dilution, as judged from the composition profiles is found to be ≈ 7 , 2.1 and 1.2mm for the MMA, TIG and laser processes respectively, and scales with the nominal levels of heat input (≈ 920 , 660 and 240J/mm for MMA, TIG and laser deposits respectively). The heat input determines to a large extent the level of penetration so that the results are not surprising, but a consequence of this is that the zones of plate martensite which form in the diluted regions near the fusion boundary, decrease in the order MMA→TIG→laser deposit (Fig. 10.4). Fig. 10.4b illustrates the typical bursts of martensitic transformation associated with the interdendritic regions near the fusion boundary. Such martensite is known to be detrimental^(10,11) since its formation is associated with internal stresses which adversely influence tensile and fatigue strength, and if exposed to the surface, the corrosion resistance. It should be noted that in the diluted regions where the zones of plate martensite are found, the martensite has a body-centered tetragonal crystal structure and is not hcp martensite; this is consistent with the lower concentration of cobalt in the diluted regions.

The microanalytical data discussed above were obtained along the weld centerline; it is however feasible that the dilution varies along the fusion boundary, since temperature and surface tension variations can give rise to systematic flows (Fig. 10.5a) within the melt pool,⁽¹²⁻¹⁷⁾ in the absence of excessive turbulence. Microanalysis experiments were therefore conducted along the fusion boundary, and the results are presented in Fig. 10.5. It is evident that for the laser clad samples, consistent with the nature of the expected flow pattern (Fig. 10.5a), the composition variation is symmetrical about the centerline with the least dilution associated with the centerline and the edges of the weld. The variations are not as well defined for the arc welds (Figs 10.5),

perhaps due to a greater amount of turbulence associated with these processes; the TIG weld in particular shows the greatest uniformity of composition along the fusion boundary.

It is notable that in all the welds, the extent of the dilution was always found to be less than the height of the deposit relative to the base plate, so that the height can in principle be reduced without influencing the properties of the surface.

Finally, the distribution of tungsten was examined using atomic number contrast on a scanning electron microscope, since this element partitions strongly into the liquid during solidification. In Fig. 10.6, the interdendritic regions which appear bright are rich in tungsten; all processes revealed similar levels of segregation (Figs. 10.3, 10.6). Tungsten segregation has been shown to be an important factor in influencing the carbide distribution in cobalt-based alloys; the enriched regions encourage the eventual formation of an inhomogeneous distribution of tungsten-rich carbides.⁽¹⁸⁾

10.3.2 The Scale of the Microstructure

Metallographic examination of the top layer of each deposit showed that the primary dendrite arm spacing decreases with the welding process in the order MMA, TIG and laser cladding (Fig. 10.7). Judging from the well established inverse relationship between dendrite arm spacing and the cooling rate during freezing,⁽¹⁷⁾ it can be concluded that the freezing rate also increases in the same order. For reasons which are not clear, the dendrites in the laser deposit are also noticeably more isotropic and uniform in shape (Fig. 10.7c); the explanation may lie in the fact that during solidification, the nucleation rate of dendrites is expected to be higher with welds deposited at higher cooling rates, so that impingement between adjacent dendrites stifles the development of highly anisotropic morphologies.

Microhardness tests were carried out on the matrix phase (the indentations being measured using scanning electron microscopy); the microhardness was found to increase with a decrease in the scale of the microstructure, which in turn reflects the increase in freezing rate associated with each process (Fig. 10.8). As is evident from the fine scale microanalytical data presented in Fig. 10.9 (and Table 10.5), there is no significant difference in the level of solid solution strengthening between the welds, so that the increase in matrix microhardness, and the parallel increase in macrohardness (Fig. 10.8) are attributed to the refinement of microstructure with increasing cooling rate. For the laser clad deposit, it is also evident that the base plate hardness in the vicinity of the fusion boundary has increased substantially. This is consistent with the higher cooling rates associated with laser cladding, causing the heat affected zone to transform into martensite.

10.3.3 Electron Microscopy

Thin foil specimens prepared from the top layers of each deposit in all cases revealed the same major microstructural constituents for all the welds, i.e., cobalt-rich fcc dendrites with a eutectic mixture of M_7C_3 carbides and the fcc phase (Fig. 10.10). Transmission electron

microscopy confirmed that the scale of the microstructure decreased in the order MMA, TIG and laser cladding.

The fcc matrix phase was in all cases found to contain stacking faults on $\{1\ 1\ 1\}$ planes, the stacking fault density being comparable in the laser and MMA samples, but significantly lower in the TIG sample. Table 10.5 shows that the iron concentration is highest for the TIG sample, and since iron increases the stacking fault energy of fcc cobalt,⁽¹⁹⁾ a relatively low stacking fault density is to be expected.

Within the fcc phase of a given sample, faulting seemed to be favoured on a particular variant of the four possible $\{1\ 1\ 1\}$ planes (Fig. 10.10). Making the reasonable assumption that the faults are due to mechanical deformation, the presence of residual stresses within the deposits may be responsible for the predominance of faults on a particular variant of the form $\{1\ 1\ 1\}$.

Experiments based on the contrast to be expected from different kinds of stacking faults⁽²⁰⁾ established that the faults were in all cases intrinsic in character (e.g., Fig. 10.11); this is consistent with the tendency of the fcc phase to transform to an hcp crystal structure. Intrinsic faults in effect represent a three layer thick region of hcp phase, compared with the two layer thick hcp region associated with an extrinsic stacking fault.

The MMA deposit was the only one found to contain fine $M_{23}C_6$ particles, consistent with the relatively slow cooling rate associated with this deposit (Fig. 10.12). The particles were in a cube-cube orientation with the fcc matrix (Fig. 10.12), as is usually the case with such carbides.

Electron diffraction from the M_7C_3 carbides revealed the presence of streaks (Fig. 10.13b), which have previously been thought to arise due to faults in the hexagonal structure. Recent work^(21,22) has however established that the streaking reflects the presence of boundaries between different orientations of domains of orthorhombic structure, and this was confirmed using electron diffraction (Fig. 10.13a). Fig. 10.13c shows that as expected, the streaks vanish in the $[0\ 0\ 1]$ zone, which also clearly illustrates the orthorhombic symmetry.

Finally, it should be noted that the microanalytical data (Table 10.5, Fig. 10.9) indicate that silicon partitions strongly into the matrix phase, as is the case for iron-based hardfacing alloys.^(23,24) An increase in the overall concentration of silicon could therefore lead to a change in the morphology and scale of the carbides.⁽²⁵⁾

10.4 Conclusions

Significant variations have been found in the microstructures of cobalt-based hardfacing alloys deposited using the manual metal arc, tungsten inert gas and laser cladding processes. The welds were all deposited using the typical conditions associated with each process, and for these conditions, the differences in freezing rate cause the scale of the microstructure and the degree of dilution (and the associated zones of plate martensite) to decrease in the order MMA, TIG and laser cladding. As a consequence, the strength of the microstructure decreases in the reverse order of process.

Indirect observations based on microanalysis indicate that the laser cladding process involves less turbulence within the fusion zone; the TIG deposits on the other hand are most uniform in terms of chemical composition.

The microstructure of the undiluted regions of all the alloys is, as expected, found to consist of a mixture M_7C_3 -carbide containing eutectic, between primary dendrites of a cobalt-rich fcc phase. The tendency of the latter to transform into an hcp phase is reflected in the observed propensity of intrinsic stacking faults. The distribution of the faults was found to be nonuniform, possibly due to the presence of residual stresses in all the deposits. The frequency of the faults is found to correlate with the effect of alloying elements on the stacking fault energy of the fcc phase.

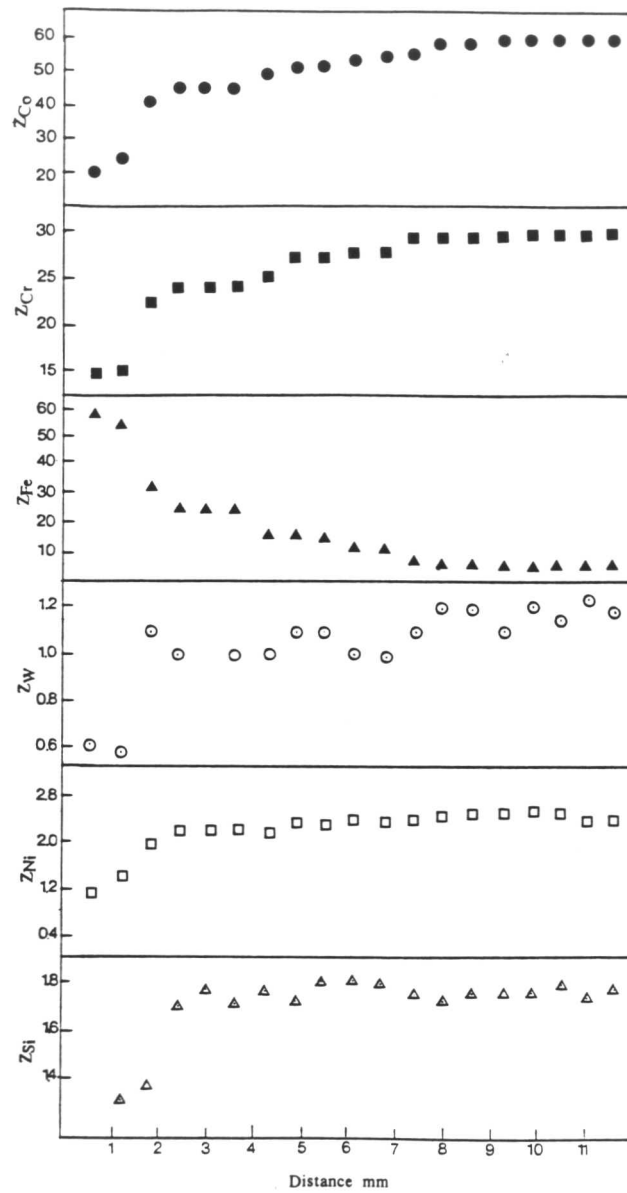
Microanalysis experiments indicated that silicon hardly dissolves in the carbide phase and this property may be of use in controlling the microstructure.

10.5 References

- 1) K. C. ANTONY: *J. of Metals*, Feb., 1983, **35**, 52.
- 2) *Metals Handbook*, 9th edn, 1983, 771, ASM, USA.
- 3) T. H. KOSEL, and N. F. FIORE: *J. Materials for Energy Systems*, 1981, **3**, 7.
- 4) V. M. DESAI, C. M. RAO, T. H. KOSEL, and N. F. FIORE: *Wear*, 1984, **94**, 89.
- 5) H. R. SHETTY, T. H. KOSEL, and N. F. FIORE: in Proc. Conf. 'Wear of Materials 1981', 1981, New York, 379.
- 6) T. H. KOSEL, N. F. FIORE, J. P. COYLE, S. P. UDVARDY, and W. A. KONKEL: in Proc. Conf. 'Corrosion-Erosion Behavior of Materials', St. Louis, Missouri, October 1978, Metallurgical Society of AIME, 190.
- 7) P. M. KELLY, A. JOSTSONS, R. G. BLAKE, and J. G. NAPIER: *Phys. Stat. Sol.*, 1975, **31**, 771.
- 8) *Welding Handbook*, 7th edn, **79**, 1981, Am. Welding Soc. FL.
- 9) G. J. BRUCK: *J. of Metals*, Feb., 1987, 10.
- 10) C. P. COOKSON: *Surfacing J.*, 1985, **16**, 125.
- 11) Z. BABIAK: *Surfacing J.*, 1985, **16**, 114.
- 12) G. E. POSSIN, H. G. PARKS, and S. W. CHIANG: in Proc. Conf. 'Laser and Electron Beam Interactions and Materials Processing', Boston, November 1980, 73.
- 13) S. M. COPLEY, D. BECK, and O. ESQUIVEL: in the 'Materials Research Society Proceedings of Laser-Solid Interactions and Laser Processing', **50**, 1978, 161.
- 14) T. CHANDE, and J. MAZUMDER: *Appl. Phys. Lett.*, 1982, **41**, (1), 42.
- 15) C. CHAN, J. MAZUMDER, and M. M. CHEN: *Metall. Trans. A*, 1984, **15A**, 2175.
- 16) T. CHANDE, and J. MAZUMDER: *J. Appl. Phys.*, 1985, **57**, (6), 2226.
- 17) H. JONES: 'Rapid Solidification of Metals and Alloys', 1982, The Institution of Metallurgists.
- 18) S. HAMAR-THIBAUT, M. DURAND-CHARRE, and B. ANDRIES: *Metall. Trans. A*, 1982, **13A**, 545.
- 19) T. SIMS: *J. of Metals*, Dec., 1969, **21**, (12), 27.
- 20) P. HIRSCH, A. HOWIE, R. B. NICHOLSON, D. W. PASHLEY and M. J. WHELAN, 'Electron Microscopy of Thin Crystals, Krieger, New York, 1977.
- 21) J. MORNIROLI, E. GROSSE, and M. GANTOIS: *Phil. Mag. A*, 1983, **48**, (3), 311.
- 22) M. KHACHFI: 'Etude Structurale des Carbures de Type M_7C_3 et Des Borures de Type M_7B_3 ', PhD. Thesis, 1986, Institut National Polytechnique de Lorraine.
- 23) L. SVENSSON, B. GRETOFT, B. ULANDER, and H. K. D. H. BHADSHIA: *J. of Materials Science*, 1986, **21**, 1015.
- 24) S. ATAMERT, and H. K. D. H. BHADSHIA: in Proc. Conf. 'Heat Treatment 87', May 1987, The Institute of Metals.
- 25) W. S. OWEN: *Trans. A. S. M.*, 1954, **46** 812.

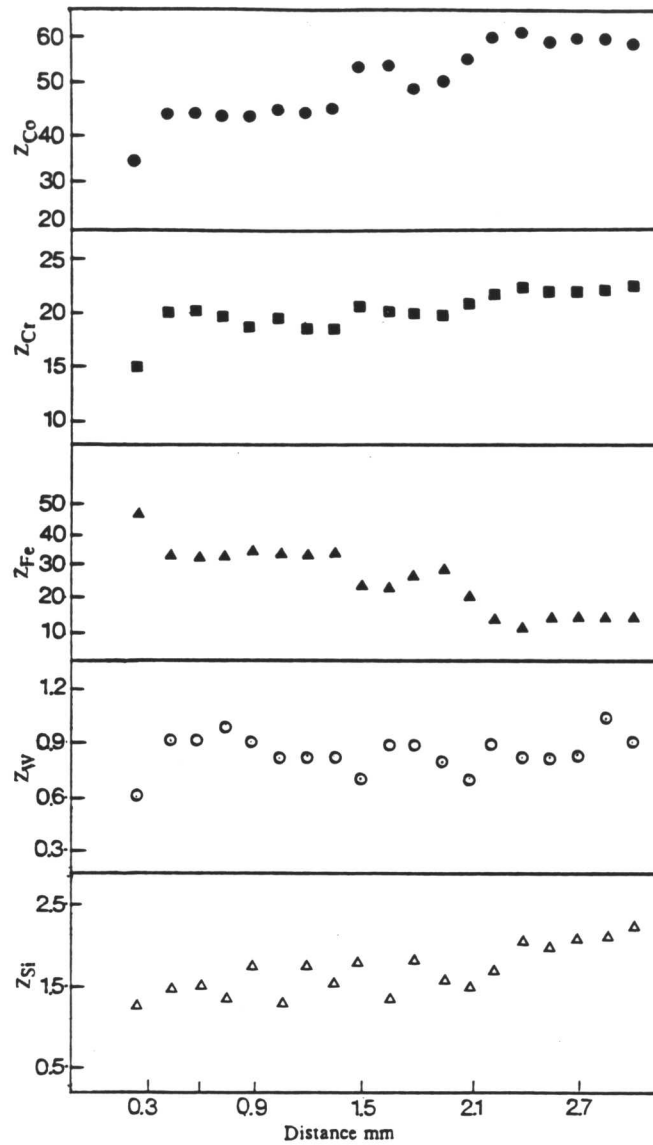
Table 10.5: Microanalytical data obtained using transmission electron microscopy and energy dispersive X-ray analysis. Z refers to the atomic percent calculated without taking account of the presence of carbon. Notice that Z is very nearly the same as the actual atomic percent for the matrix, since the amount of carbon in the matrix is rather small, but for the carbide, Z will represent an overestimation of the actual atomic percent by a factor (1/0.7), assuming that the M_7C_3 carbide is stoichiometric.

	Matrix			M_7C_3		
	MMA	TIG	Laser	MMA	TIG	Laser
Z_{Co}	53.3	56.7	58.9	11.65	14.4	15.7
Z_{Cr}	28.3	24.4	24.9	82.7	76.6	75.7
Z_W	1.0	0.87	0.9	1.47	2.77	2.38
Z_{Fe}	12.0	15.8	11.7	4.2	6.03	4.54
Z_{Mn}			1.34			1.66
Z_{Si}	2.6	2.23	2.26	0.02	0.2	0.02
Z_{Ni}	2.8			0.11		



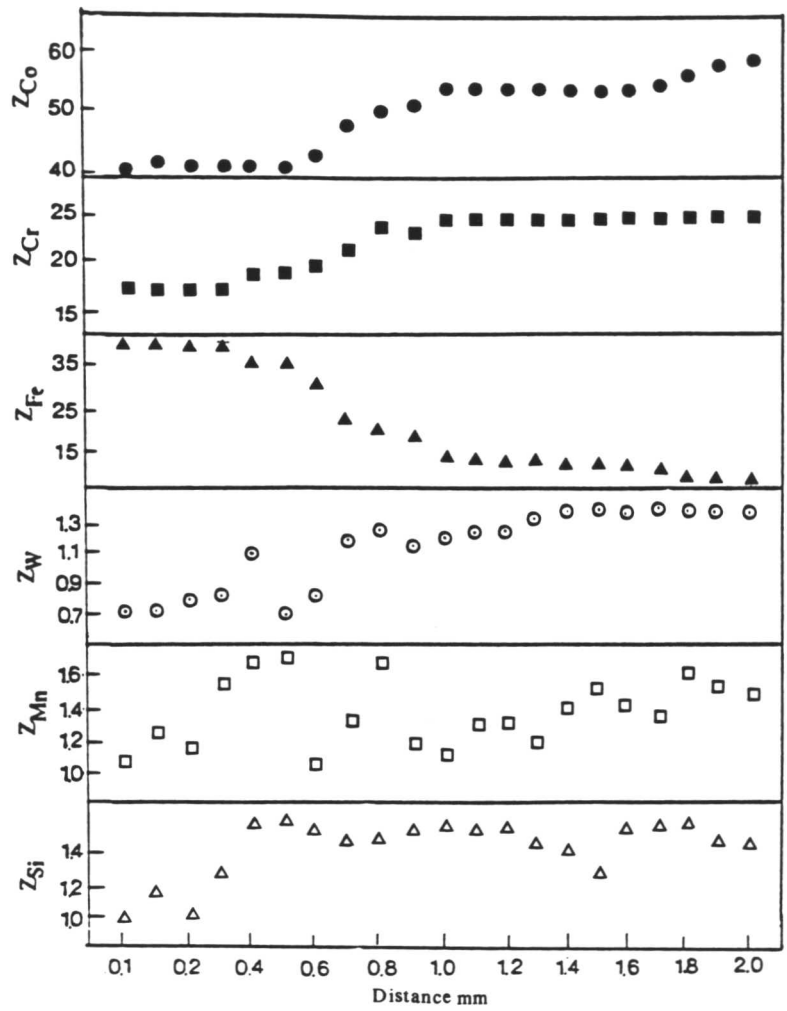
a

Fig. 10.3: Microanalysis experiments carried out using scanning electron microscopy and energy dispersive X-ray analysis. The scans are carried out across the fusion boundary between the base-plate and the first layer, along the centerline of the weld. (a) MMA; (b) TIG; (c) Laser cladding.



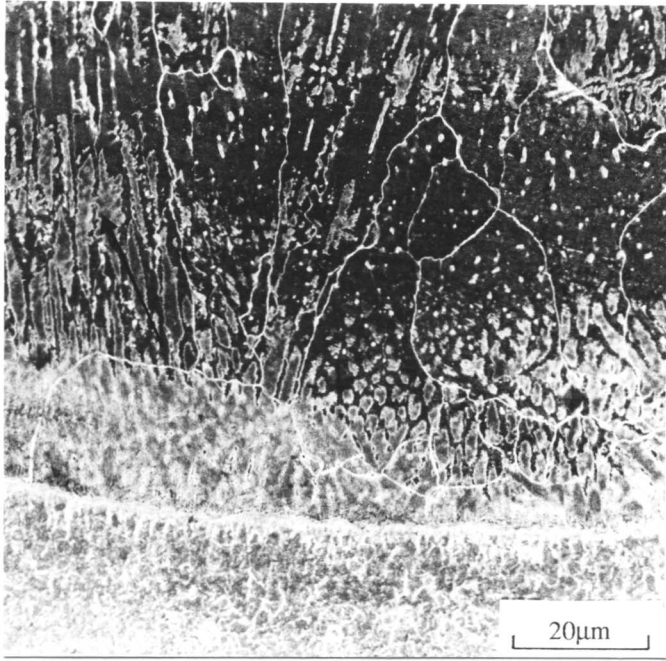
b

Fig. 10.3: Microanalysis experiments carried out using scanning electron microscopy and energy dispersive X-ray analysis. The scans are carried out across the fusion boundary between the base-plate and the first layer, along the centerline of the weld. a) MMA; b) TIG; c) Laser cladding.

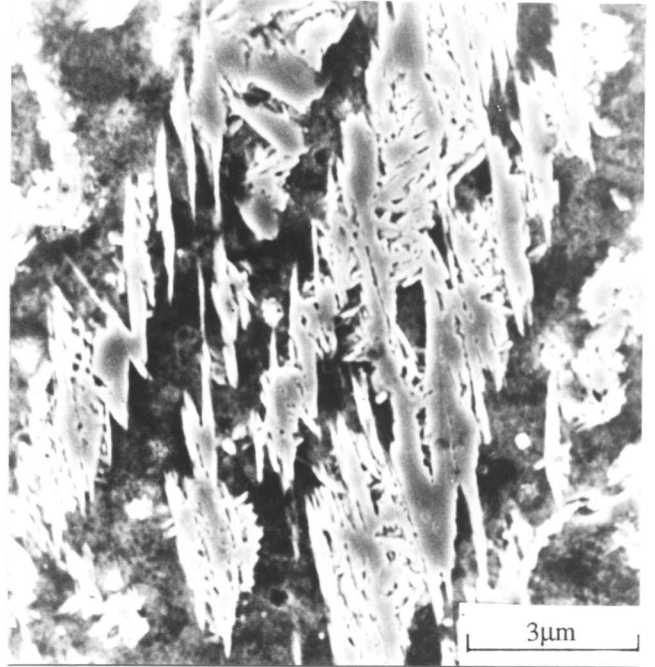


c

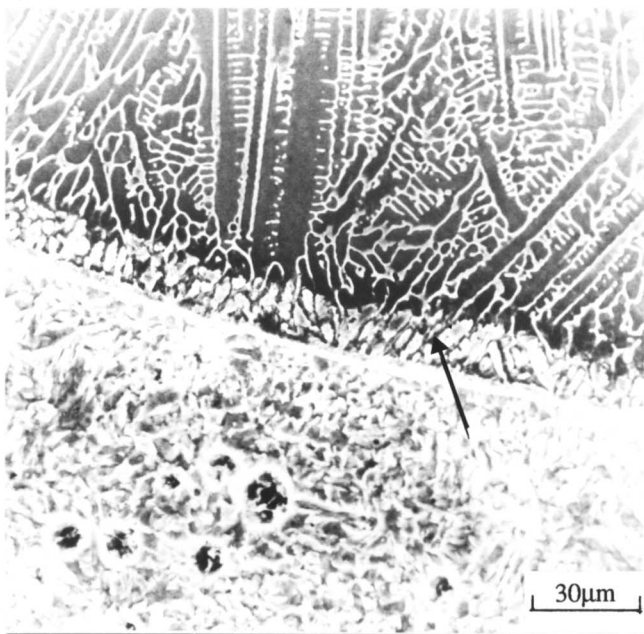
Fig. 10.3: Microanalysis experiments carried out using scanning electron microscopy and energy dispersive X-ray analysis. The scans are carried out across the fusion boundary between the base-plate and the first layer, along the centerline of the weld. a) MMA; b) TIG; c) Laser cladding.



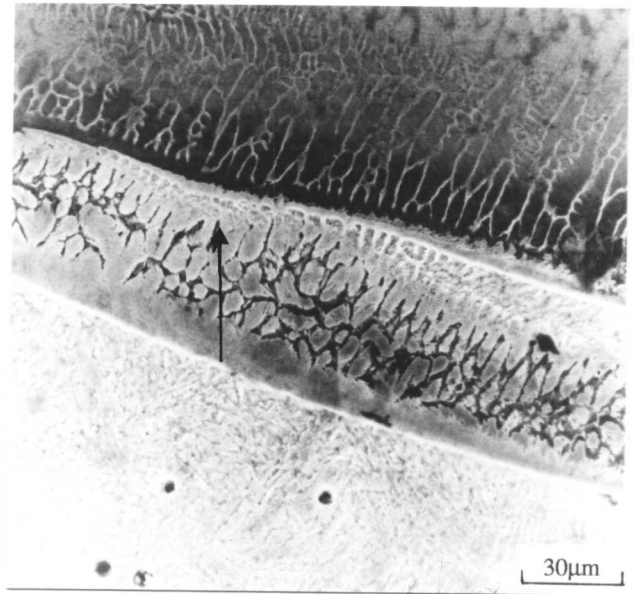
a



b

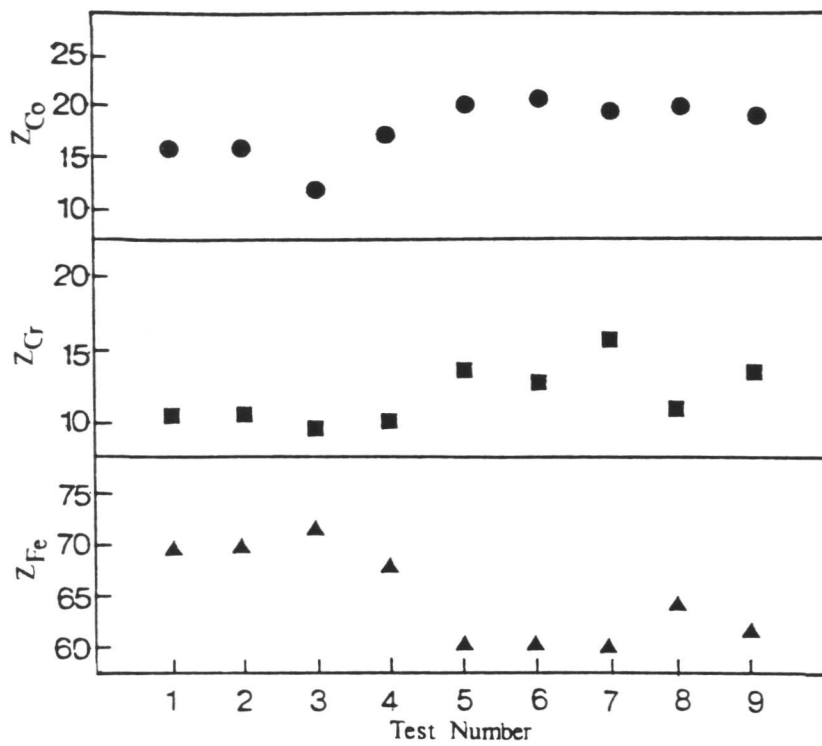
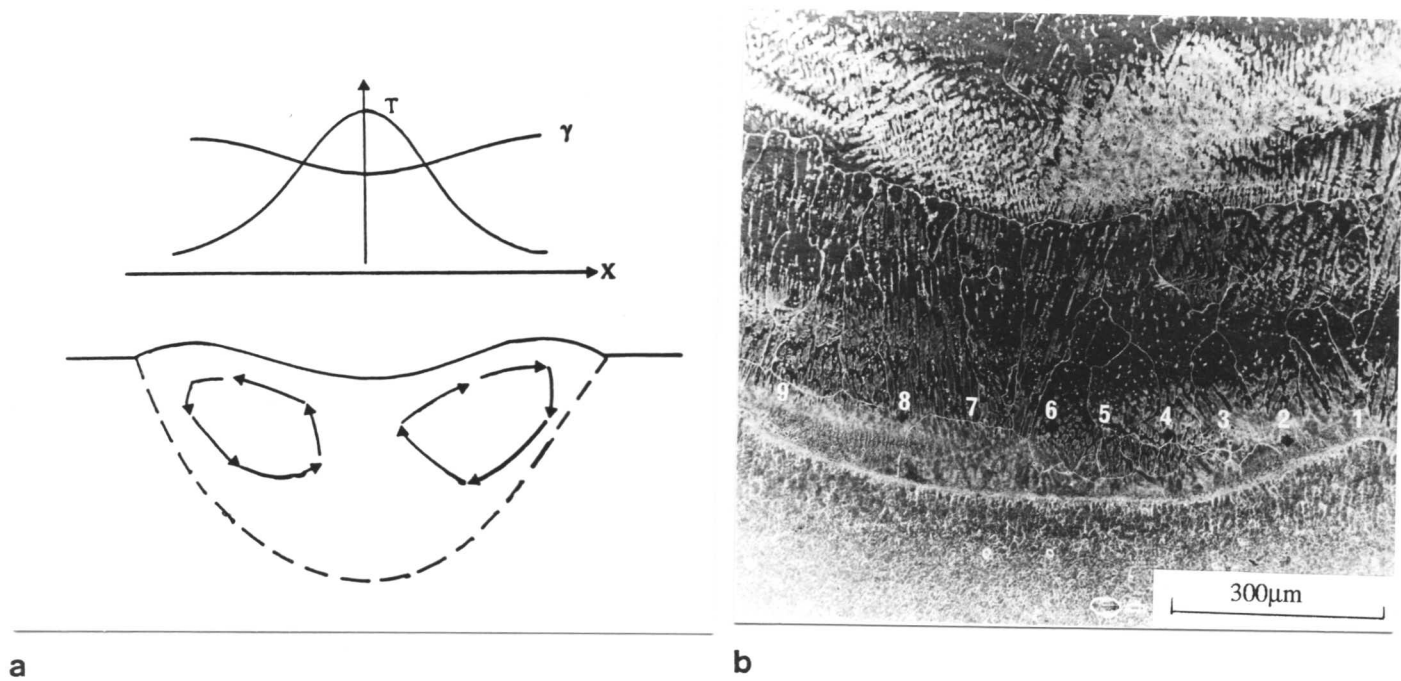


c

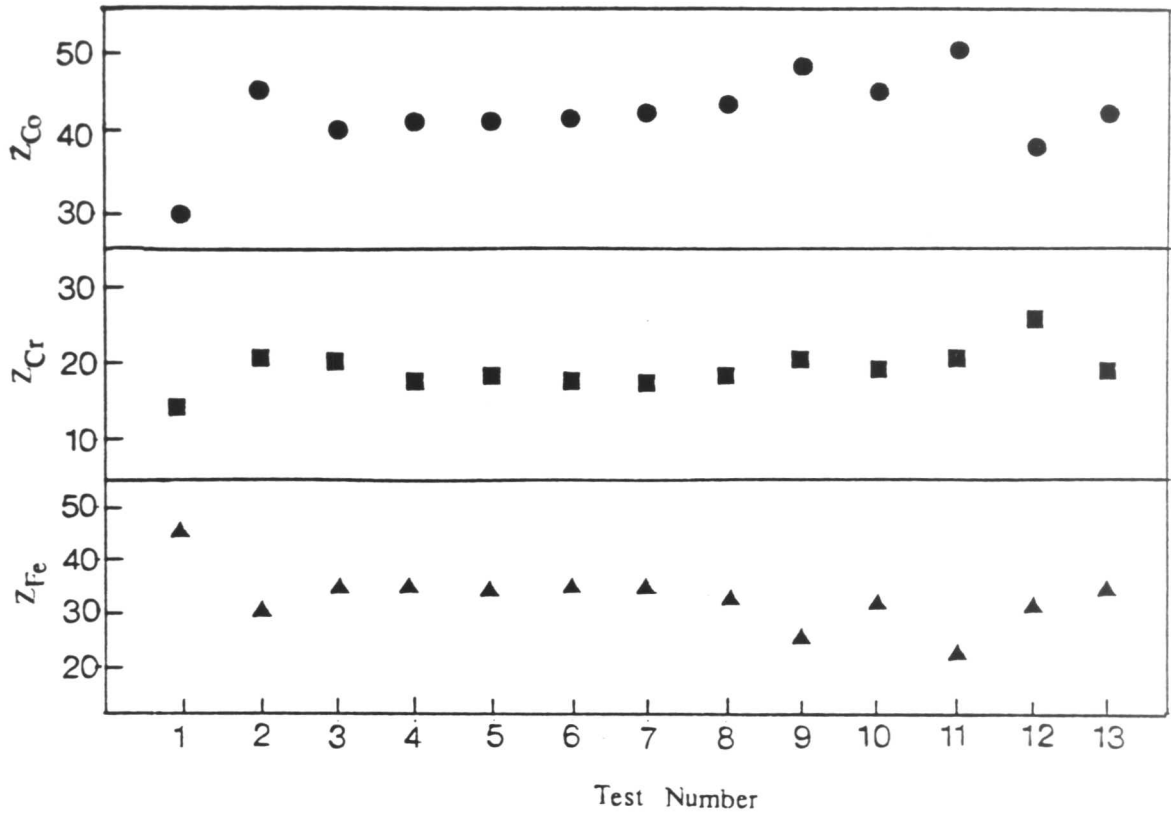
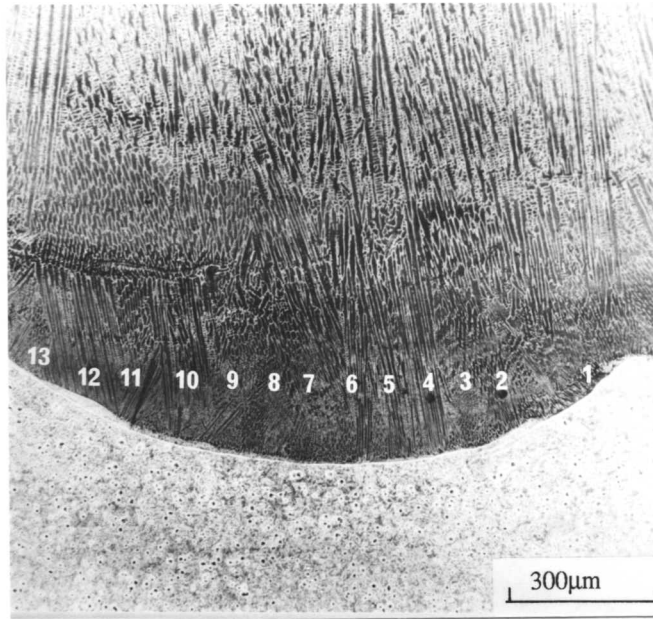


d

Fig. 10.4: Scanning electron micrographs illustrating the zones of martensite (indicated by arrows) that form in regions of high dilution. a) MMA; b) higher magnification image of the MMA deposit; c) TIG; d) Laser cladding.

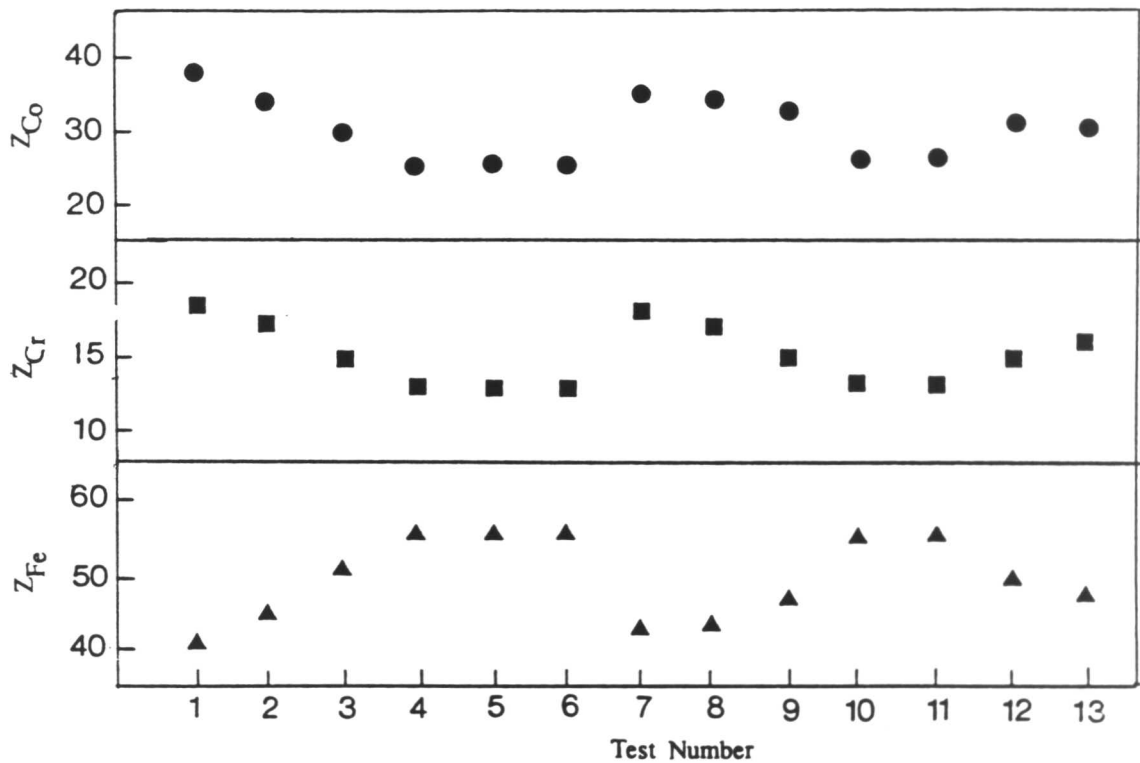
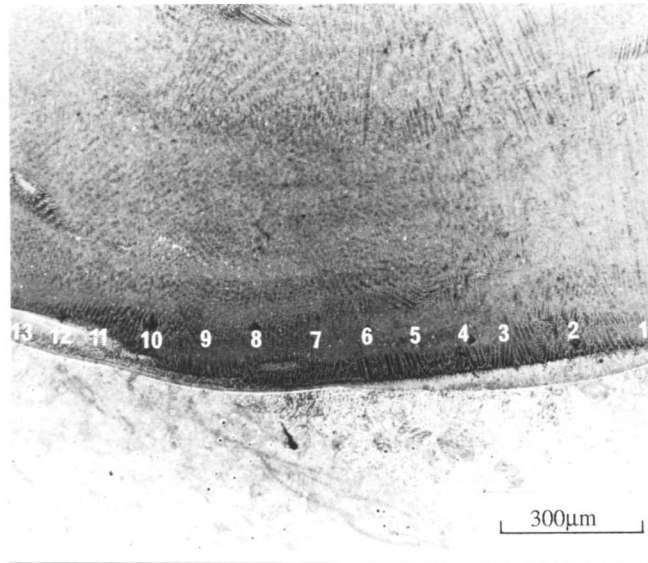


b
 Fig. 10.5: a) Schematic diagram illustrating the nature of the surface tension driven flow within the fusion zone, where γ is the surface tension and T is the temperature; (b-d) microanalysis experiments carried out using scanning electron microscopy and energy dispersive X-ray analysis. The scans are carried out along the fusion boundary between the base-plate and the first layer, at positions illustrated in the micrographs. b) MMA; c) TIG; d) Laser cladding.

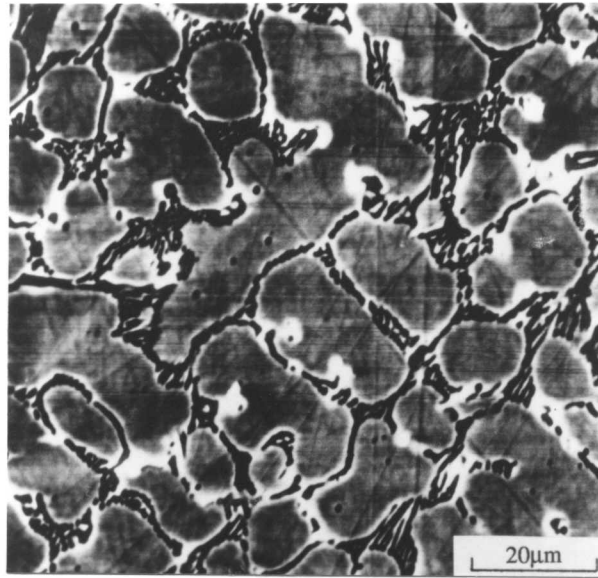


c

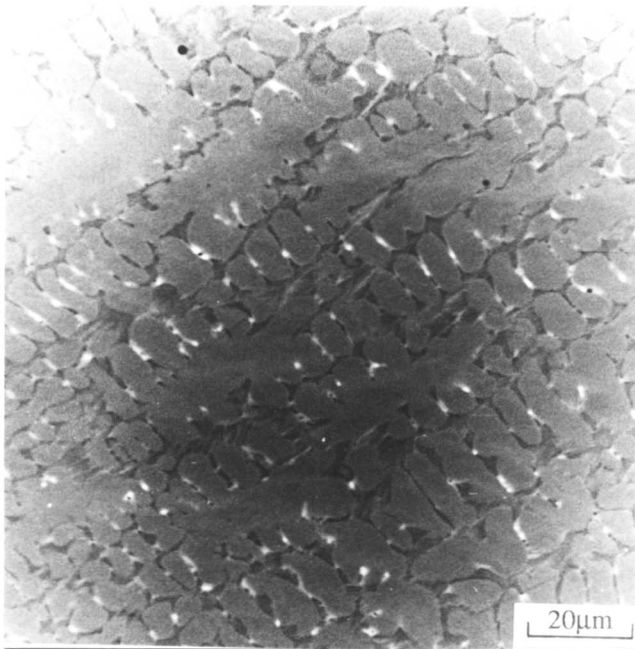
Fig. 10.5: a) Schematic diagram illustrating the nature of the surface tension driven flow within the fusion zone where γ is the surface tension and T is the temperature; (b-d) microanalysis experiments carried out using scanning electron microscopy and energy dispersive X-ray analysis. The scans are carried out along the fusion boundary between the base-plate and the first layer, at positions illustrated in the micrographs. b) MMA; c) TIG; d) Laser cladding.



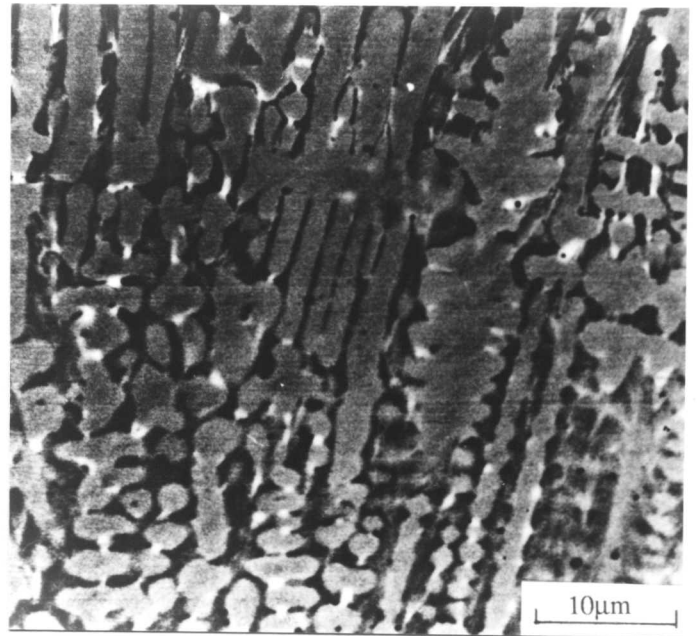
d Figure 10.5: a) Schematic diagram illustrating the nature of the surface tension driven flow within the fusion zone where γ is the surface tension and T is the temperature; (b-d) microanalysis experiments carried out using scanning electron microscopy and energy dispersive X-ray analysis. The scans are carried out along the fusion boundary between the base-plate and the first layer, at positions illustrated in the micrographs. b) MMA; c) TIG; d) Laser cladding.



a

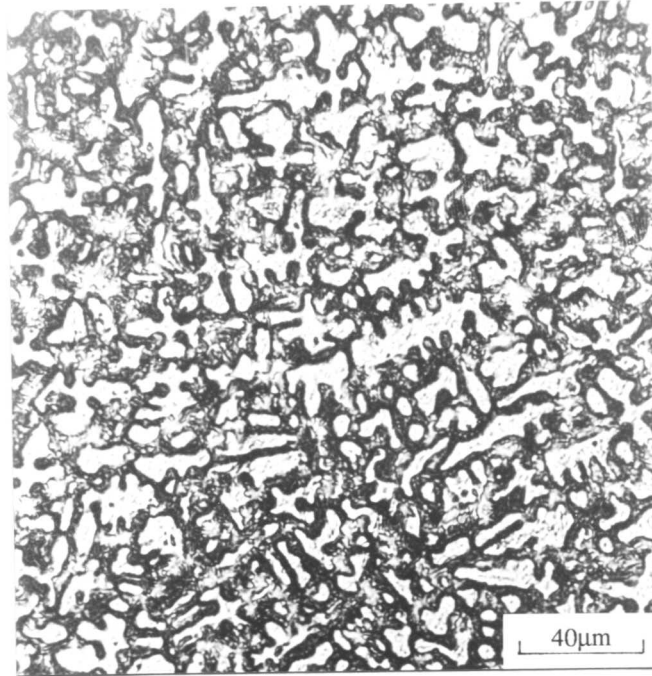


b

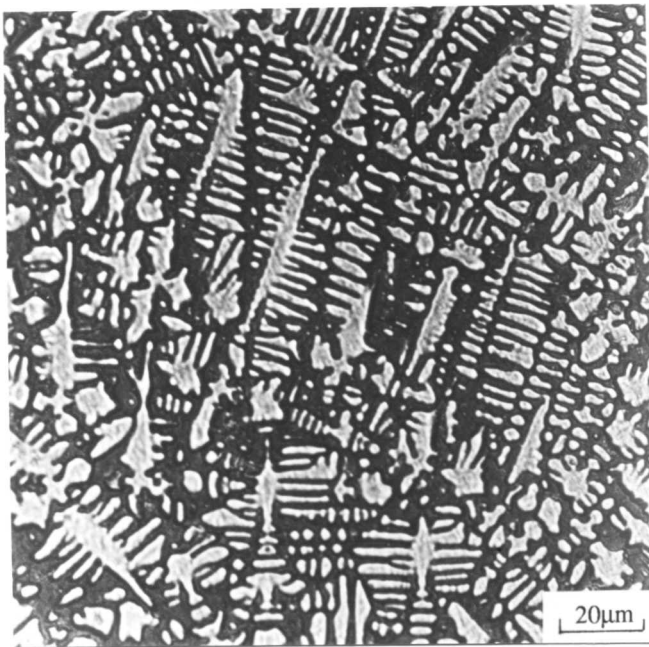


c

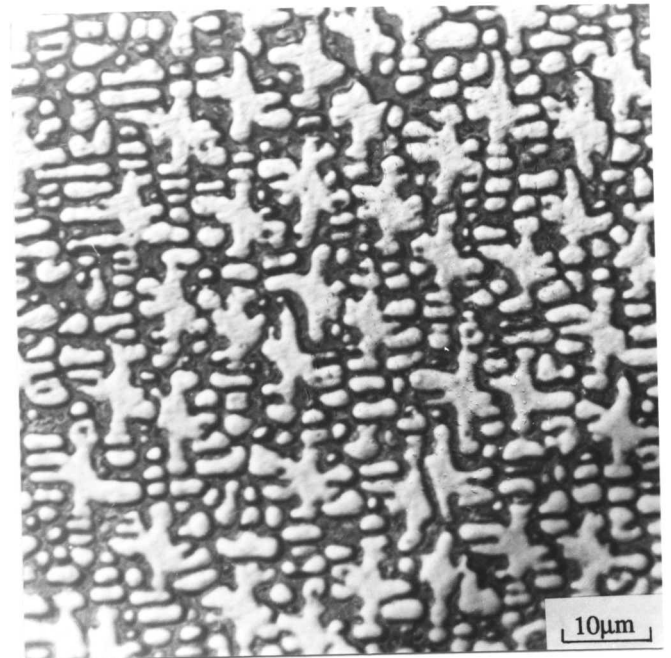
Fig. 10.6: Scanning electron micrographs of polished specimens, using atomic number contrast, to reveal the distribution of tungsten in the a) MMA; b) TIG; c) laser deposits. The bright regions are tungsten-rich.



a

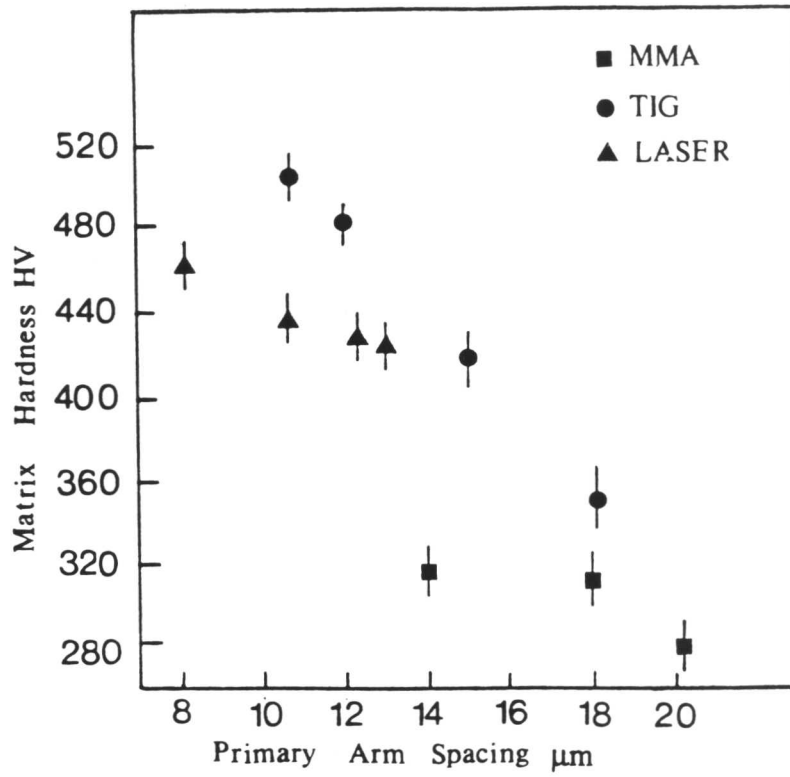


b

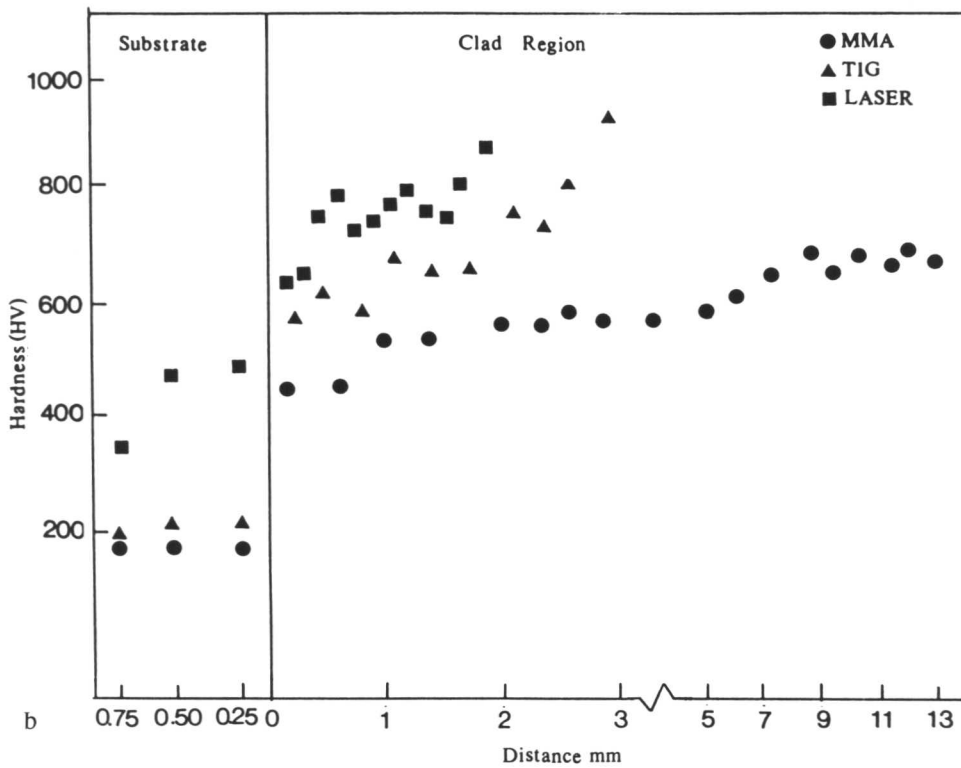


c

Fig. 10.7: Light optical micrographs (longitudinal sections) illustrating the scale of the microstructure in the top layers of the hardfacing deposits. a) MMA; b) TIG; c) laser cladding.

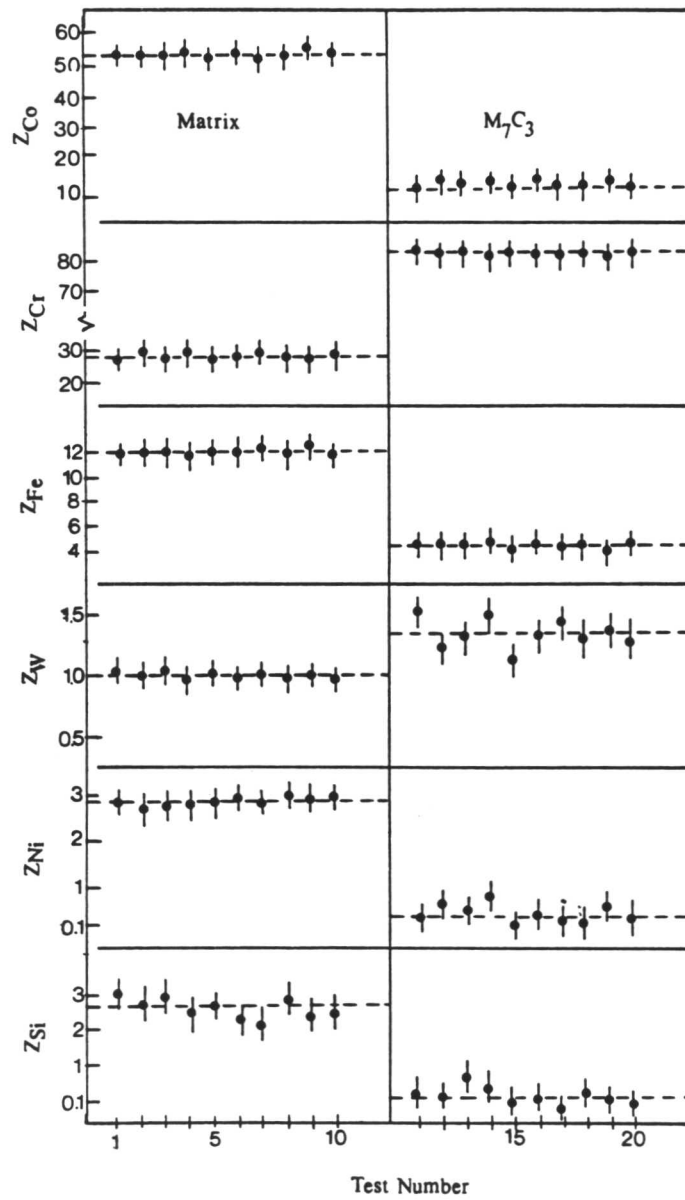


a



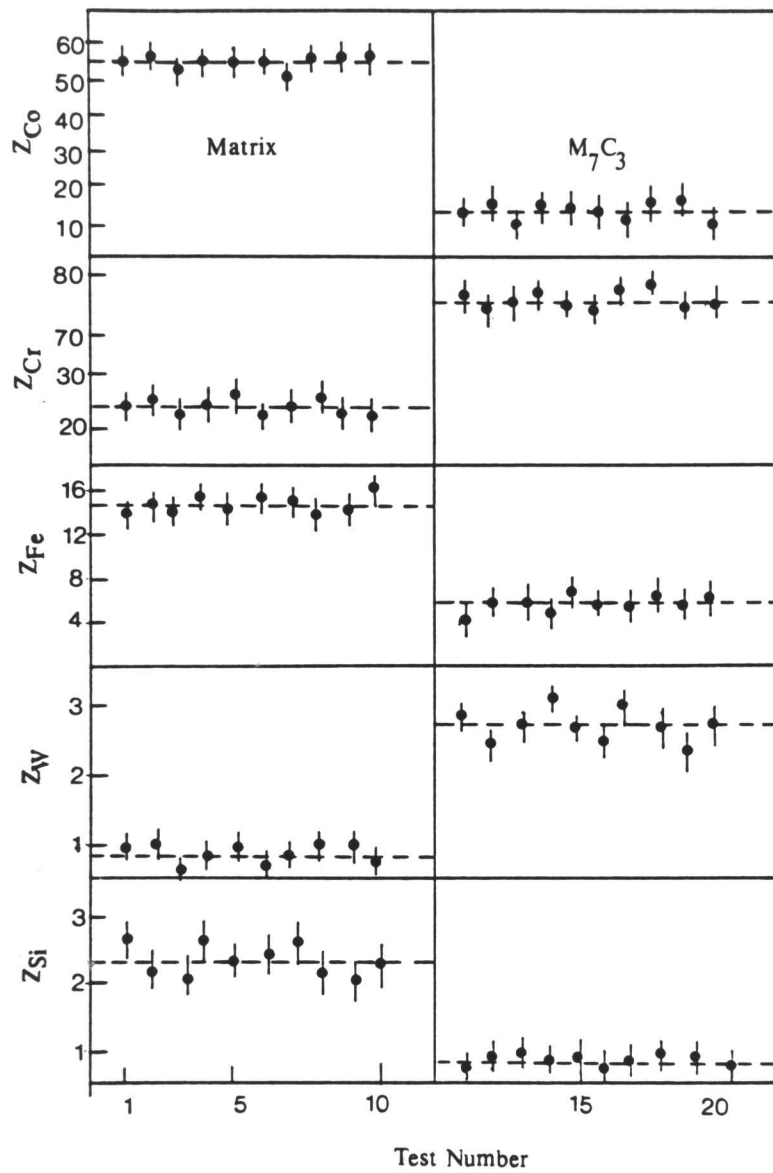
b

Fig. 10.8: a) Variations in the microhardness of the cobalt-rich fcc matrix phase with primary arm spacing. The experimental scatter is represented by the error bars; b) variations in the macrohardness throughout the each deposit.

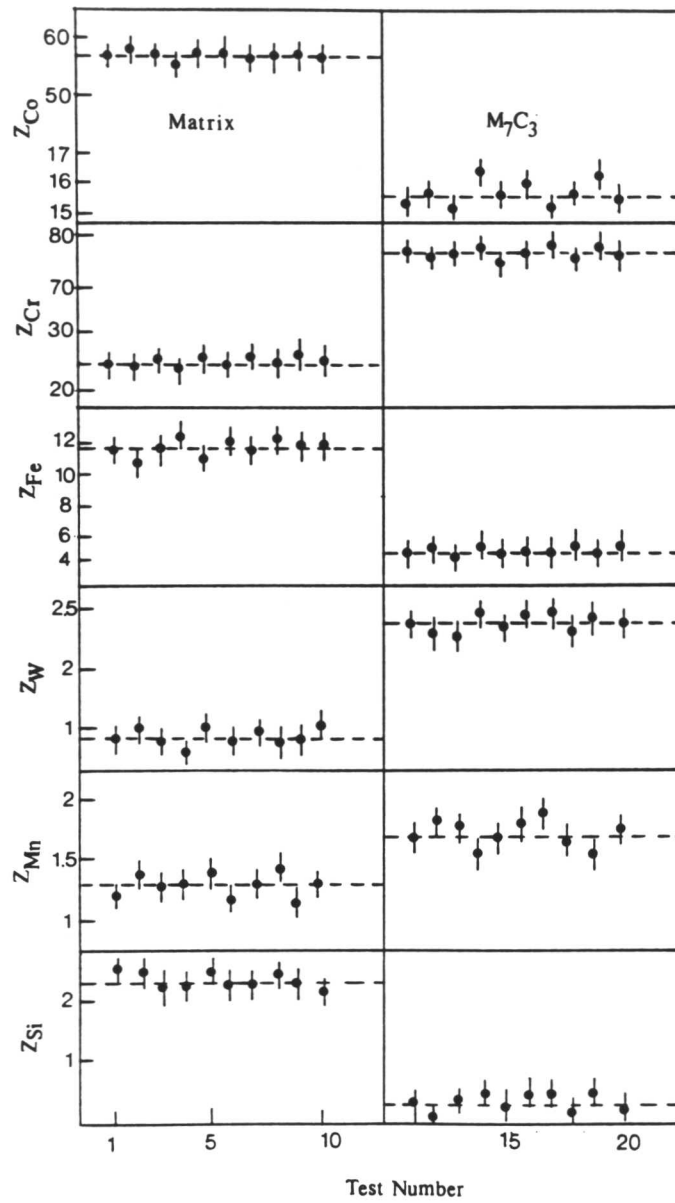


a

Fig. 10.9: Microanalysis experiments carried out using transmission and scanning transmission electron microscopy and energy dispersive X-ray analysis. a) MMA; b) TIG; c) laser cladding.



b
 Fig. 10.9: Microanalysis experiments carried out using transmission and scanning transmission electron microscopy and energy dispersive X-ray analysis. a) MMA; b) TIG; c) laser cladding.

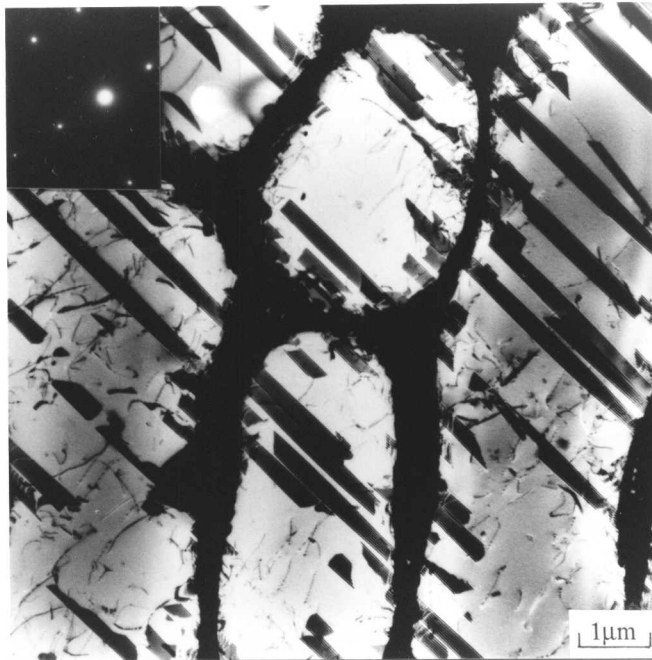


C

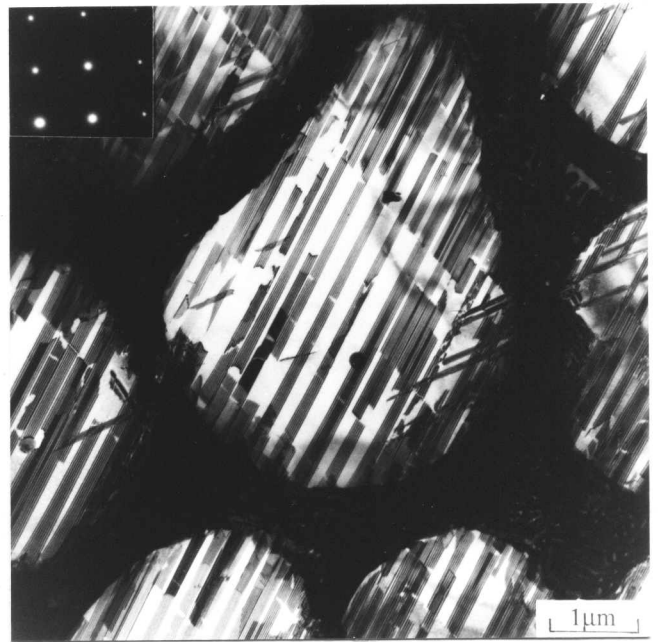
Fig. 10.9: Microanalysis experiments carried out using transmission and scanning transmission electron microscopy and energy dispersive X-ray analysis. a) MMA; b) TIG; c) laser cladding.



a



b



c

Fig. 10.10: Bright field transmission electron micrographs from the top layers of each deposit. a) MMA; b) TIG; c) laser cladding. The diffraction patterns in the insets show that the cobalt-rich matrix is fcc in crystal structure; the zone axes of the patterns are $\langle \bar{1} 1 4 \rangle$, $\langle \bar{1} 1 3 \rangle$, and $\langle 0 0 1 \rangle$ respectively.

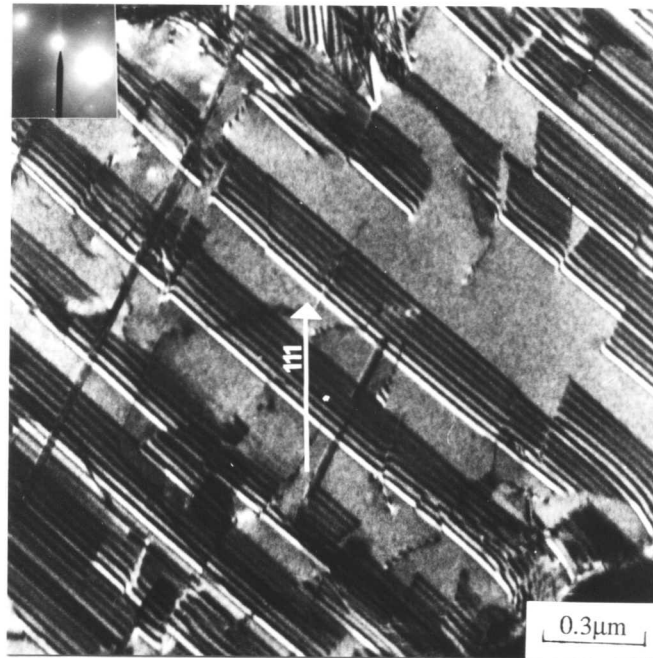


Fig. 10.11: Dark field transmission electron micrograph from the top layer of the laser clad specimen, illustrating the intrinsic character of all the stacking faults. The contrast experiment is based on the fact that if the origin of the g vector is placed at the fault center in a centered dark field image, g points away from the light outer fringe if the fault is extrinsic and towards it if is intrinsic for all $\{2\ 0\ 0\}$, $\{2\ 2\ 2\}$, $\{4\ 4\ 0\}$ type reflections. If the operative reflection is one of the type $\{4\ 0\ 0\}$, $\{1\ 1\ 1\}$, $\{2\ 2\ 0\}$ the reverse is true.

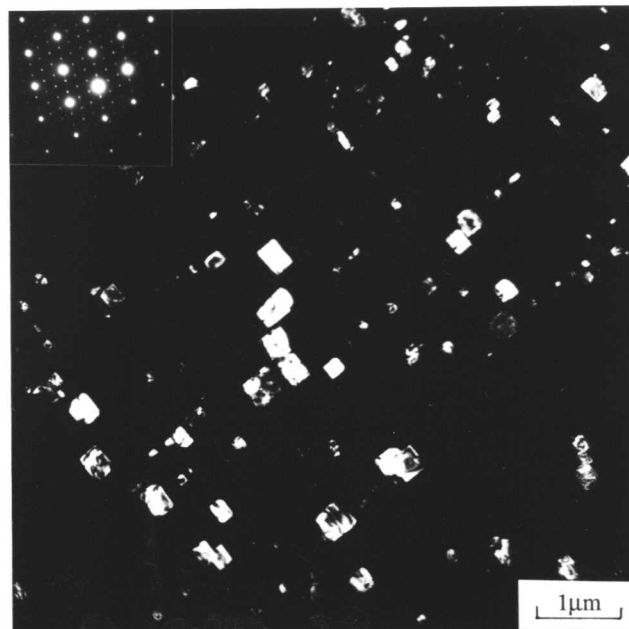
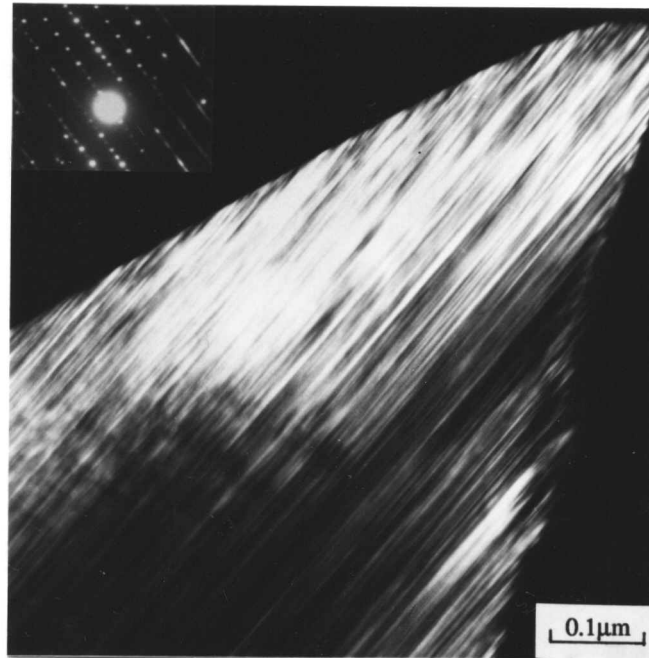
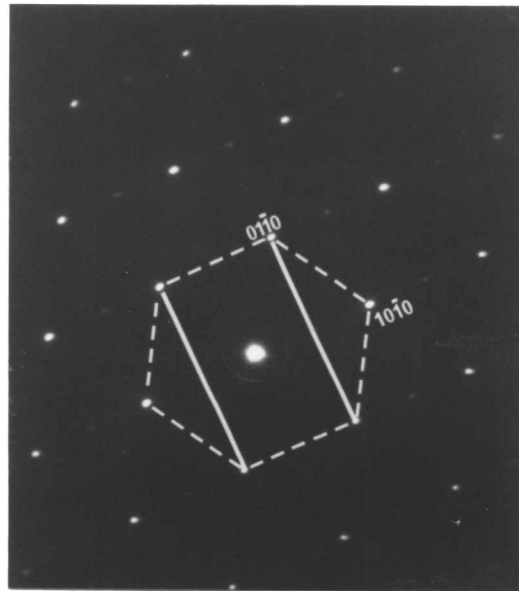


Fig. 10.12: Dark field transmission electron micrograph and corresponding electron diffraction pattern (superimposed $\langle 1\ 1\ 0 \rangle$ zones from both the matrix and carbide phases) showing the presence of $M_{23}C_6$ particles in the as-deposited MMA weld.



a



b

Fig. 10.13: a) Dark field transmission electron micrograph and corresponding electron diffraction pattern of M_7C_3 carbide in the manual metal arc weld showing streaking; b) the electron diffraction pattern has a $\langle 001 \rangle$ zone axis illustrating the orthorhombic symmetry.

11. COMPARISON OF THE ABRASIVE WEAR PROPERTIES OF STELLITE HARDFACING ALLOYS DEPOSITED BY ARC WELDING AND LASER CLADDING

By S. Atamert and H K J H Bhadeshia

11.1 Introduction

In Chapter 10 the presence of systematic microstructural and microanalytical differences were demonstrated between Stellite cobalt-based hardfacing alloys deposited by manual metal arc welding, tungsten inert gas (TIG) welding and laser cladding, using typical process parameters. As a consequence of the differences in nominal heat input (920, 660 and 240 Jmm⁻¹ for MMA, TIG and laser cladding, respectively) and associated freezing rates, the scale of the microstructure and the degree of dilution was found to decrease in the order MMA, TIG and laser cladding, with the hardness increasing in the same order. Microanalysis experiments also suggested that the TIG deposits are most uniform with respect to chemical compositions, and due to their relatively high matrix iron content, tend to be most stable to the transformation from the face-centered cubic (fcc) to hexagonal close-packed (hcp) phase. Hence, the TIG samples were to contain lower densities of intrinsic stacking faults when compared with the MMA and laser clad samples.

This chapter is an attempt to relate the differences summarised above, and the detailed differences reported in Chapter 10, between the three kinds of hardfacing deposits, to the wear properties. The aim is to attempt a rationalisation of wear behaviour as a function of microstructure and abrasive characteristics. Detailed microscopy is used to deduce the micromechanisms of wear.

11.2 Experimental Method

Most of the experimental details have been presented in Chapter 10, so that the following section deals with just the additional techniques associated with the wear analysis.

Abrasion wear tests (pin-on-disc) were performed on 3mm diameter cylindrical specimens impinging vertically on a rotating disc coated with the appropriate abrasive. The specimens were gravity loaded with a mass of 450g. The cylindrical samples were spark-machined from the weld deposits, so that the test surface was parallel to the layers of hardfacing material. The test surfaces had to be flattened by grinding in order to remove the curvature associated with the top surfaces of the weld deposits. This entailed removal of ≈ 0.5 mm of the top surface so that all tests begin at this depth below the surface.

The weight loss due to abrasive wear was measured at various intervals during the test period. The effects of two kinds of fixed-abrasives were studied using the rotating coated disc test: 280 mesh SiC, and 400 mesh Al₂O₃ with nominal particle sizes ≈ 40 and ≈ 17 μ m respectively (see Fig. 7.1). The relative velocity of the disc and sample was 0.63 m/s. This sliding speed would probably cause a local rise in temperature ahead of abrasive particles. However, in similar

circumstances, the bulk temperature has been reported to rise by only 10°C.⁽¹⁾ In any case, the effect would be applicable to all samples and consequently does not influence the comparisons between samples. In order to avoid spurious effects due to the degradation of abrasive during the wear tests, the abrasive paper was changed at 1 minute intervals. The wear tests were carried out in air under dry test conditions.

In addition to the pin-on-disc tests, single and multiple scratch tests were carried out using SiC fibres ($\approx 100\mu\text{m}$ diameter) loaded with a mass of 100g, and with a Vicker's pyramidal diamond loaded at 100, 500 and 1000g. The scratch tool was in each case mounted at the end of a balanced parallelogram arm instrumented with strain gauges and loaded by gravity. The specimen was then moved linearly by a geared electric motor at a speed of 0.25mms^{-1} for a distance of 7mm.

The worn surfaces were ultrasonically cleaned and then examined using a scanning electron microscope. Thin foil samples for transmission electron microscopy were prepared as in Chapter 10, but the aim here was to examine the fine structure in the vicinity of abraded surfaces. The samples were extracted by slicing parallel to the abraded surfaces, lightly levelling the abraded surface with 1200 mesh SiC polishing paper, and then grinding back from the opposite surface to reach a thickness suitable for electropolishing. The levelling may have caused some additional deformation. However, the use of the much finer SiC, the wet conditions and the light pressure should ensure that any additional deformation effect is small. It is estimated that the samples examined represent a depth of about 0.6mm below the abraded surface concerned.

11.3 Results and Discussion

11.3.1 Pin-on-Disc Abrasion Tests

11.3.1.1 Alumina Abrasive

It is well established that variations in wear resistance are related to the difference in hardness of the abrasive and resisting surfaces. If the difference is small, the rate of material removal during abrasion is found to be very low when compared with the case where the abrasive is relatively hard.⁽²⁾ The critical value of the ratio of the abrasive hardness to that of the strained hardened metal surface (H_a/H_m) has been estimated empirically as 1.2, below which an effective increase in wear resistance is observed.⁽³⁾

In the present study, Al_2O_3 and SiC abrasives were chosen in order to compare the effect of the hardness and the size of the abrasives and to examine material removal mechanisms under each abrasive. The hardness of Al_2O_3 , SiC and $(\text{Fe}, \text{Cr})_7\text{C}_3$ is 2100, 2480-2600 and 1200-1600 HV respectively.^(4,5)

Weight loss versus time curves of the abrasion test results with the Al_2O_3 abrasive for the MMA, TIG and laser clad samples are given in Fig. 11.1a with corresponding worn surface micrographs being presented in Figs. 11.1b-e. The mean wear rates of the MMA, TIG and laser

clad samples are found to be 0.0068, 0.0029 and 0.0032 g/min. The results show that the MMA weld has the poorest abrasive wear resistance among the three deposits, with a wear rate which remains constant throughout the test, unlike the other two samples which at least initially exhibited a decreasing wear rate with time.

Although the TIG sample initially showed a lower net weight loss when compared with the laser clad sample, its wear rate was found to increase significantly after 4 minutes of abrasion. In fact, the ultimate weight losses for the TIG and laser clad samples were observed to be similar. The observed rise in wear rate towards that end of the test, for both the TIG and laser clad samples corresponds approximately to the point where it is the diluted regions of the deposit which are being abraded, since the undiluted layers have then been completely eroded. Hence, the design life of the cladding should strictly be calculated on the basis of the undiluted layer thickness.

Scanning electron microscopy (Fig. 11.1b-e) revealed that the worn surfaces of the MMA and the laser clad deposits were neatly cut by the abrasive particles, in a manner consistent with micromachining processes. The wear grooves can in these cases be seen to be continuous and smooth, indicating that the material which was originally within the grooves was neatly cut away and detached by the abrasive particles. Consistent with their higher wear rate, the grooves tended to be deeper for the MMA samples reflecting their lower starting strength. Indeed, the observed constant wear rate (i.e., the linear relationship between the weight loss and time plot) of the MMA samples is indicative of an inadequate degree of strain hardening during the abrasion test. The rate of strain hardening is known to increase as the microstructure becomes refined,⁽⁸⁾ so that the lack of sufficient strain hardening is attributed to the relative coarseness of the MMA deposit microstructure, as reported in Chapter 10.

The fact that the laser and TIG samples showed better wear resistance than the MMA sample again correlates with their higher starting hardness, and to the finer scale of their microstructures (Chapter 10). As will be discussed later, these microstructural features are also of importance in controlling the spread of deformation in the vicinity of the grooves. It is notable that only the laser sample showed an increase in wear resistance during the progress of the test: the MMA sample is relatively soft and has a coarse microstructure, whereas the TIG sample has a relatively high matrix stacking fault energy (corresponding to its higher matrix iron content) which leads to a lower work hardening rate.⁽⁹⁾

The TIG sample, which showed the best initial resistance to wear, also exhibited a drastically different worn surface morphology (Fig. 11.1d,e). The relatively discontinuous grooves are in this case not formed by pure cutting, the material exhibiting clear resistance to the passage of the abrasive particles. Material debris can be seen to be piled up at intervals, apparently at positions within the grooves where the motion of the abrasive particles has been stifled. The alloy clearly behaves in a more ductile manner so that the micromachining debris does not readily detach from the test surface and hinder the wear process. The higher ductility relative to the laser sample

cannot be attributed to the minor difference in the scale of the two microstructures. It is more likely that the laser sample, due to its lower matrix stacking fault energy, strain hardens rapidly so that its harder debris easily detaches during wear, giving rise to "free machining" behaviour. Due to its higher matrix iron concentration, the TIG samples have a higher stacking fault energy and consequently strain harden to a lesser degree, giving a more ductile machining behaviour.

11.3.1.2 Silicon Carbide Abrasive

Similar experiments were carried out using the harder ($\approx 2480\text{-}2600\text{HV}^{(4,5)}$) SiC abrasive. Weight-loss versus time curves, and scanning electron microscope observations of the final worn surfaces are given in Fig. 11.2. The results are clearly different from the case where the abrasive particles were alumina: the samples this time show more similar wear rates, the mean values of which are 0.0100, 0.0094 and 0.0086 g/min for the MMA, TIG and laser clad specimens respectively. Apart from minor fluctuations, they all exhibit an approximately constant wear rate during the test, although the laser samples start off with slightly lower wear rate, perhaps a reflection of their strain hardening capacity. Consistent with these observations, the wear surfaces (Fig. 12.2b-d) all show neat, continuous grooves with the samples offering little resistance to the passage of abrasive particles. Clearly, the use of a SiC abrasive has wiped out most of the differences between the three kinds of samples. The wear rates obtained with the SiC abrasive is higher than that with Al_2O_3 abrasive. This can be attributed to two effects, the most important of which is the size effect.⁽⁷⁻¹³⁾ The abrasives used in this study are in a size range where the wear rate increases with abrasive size; the SiC abrasive is coarse compared with the alumina. The higher hardness of SiC may also contribute to its more aggressive abrasion properties, but this is likely to be a smaller effect since both SiC and Al_2O_3 have a significantly higher hardness when compared with the phases present in the Stellite deposits. It is estimated that in the case of the laser and TIG samples, the top, undiluted layers are removed completely after about 2-3 minutes of testing.

11.3.2 Transmission Electron Microscopy

Thin foils for transmission electron microscopy were prepared directly from the abraded surfaces, after the pin-on-disc tests carried out using SiC abrasives. The metallographic results presented here are representative of three samples examined from each of the abraded deposits. Nonetheless, it is recognised that the observations reported here are essentially qualitative and are intended to reflect the broad trends in deformation behaviour.

The results are illustrated in Figs. 11.3-11.5. The matrix (originally of face-centered cubic structure) regions of the MMA and laser clad deposits were found to contain numerous platelets of hexagonal close-packed structure, due to stress induced fcc \rightarrow hcp transformation. The frequency of occurrence of the platelets was highest for the laser clad samples. This contrasted with the TIG samples, which seemed to contain much more dislocation debris, with very few hcp platelets, although twinned fcc regions could often be observed. The behaviour of the TIG sample is as

expected, since its matrix phase has a high stacking fault energy corresponding to its relatively high iron content.

The fact that the MMA deposits contain a lower density of hcp platelets relative to the laser samples is at first sight confusing since the matrix chemical compositions of the two samples are very similar. However, the MMA deposit has a lower starting hardness, and it will be demonstrated later that the deformation associated with the abrasion process extends over a larger volume for the MMA deposit (due to the coarseness of its microstructure). Both of these factors would lead to lower mean levels of stress in the material, so that a lower degree of stress induced transformation is expected. The fact that the laser clad samples are unique in exhibiting an increase in wear resistance during testing (Fig. 11.1) can now be explained, since the platelets formed by fcc→hcp transformation offer formidable obstacles to dislocation motion, leading to considerable strain hardening.

11.3.3 Scratch Tests Using Vickers Diamond

Scratch tests were carried out using a Vickers pyramidal diamond indenter with 100, 500 and 1000g loads, for all three kinds of samples, although no significant differences in abrasive behaviour were found for the different loads used. After scratching, the specimens were examined using scanning electron microscopy (Fig. 11.6). The results clearly illustrate the considerable deformation (in the form of slip bands) induced in the region adjacent to the scratches. The extent of the deformation increases with applied load (Figs. 11.6a,b). At the highest load used, 1000g, clear signs of matrix cracking were observed (Fig. 11.6c). For a given load, the degree of deformation in the vicinity of the scratch was noted to be largest for the MMA samples, consistent with their coarse microstructure (Figs. 11.6b,d,e). The slip bands were seen to be impeded by the presence of eutectic carbides, although this did not completely prevent the onset of deformation in the Co-rich matrix which was separated from the scratches by the network of eutectic carbide (Fig. 11.6). The spread of deformation occurred to a lesser degree for both the TIG and laser clad samples; while the slip bands could be seen all along the length of the scratches in the MMA samples, they tended to be discontinuous for the TIG and laser clad samples, reflecting the finer scale of the microstructure.

The critical role of the matrix in supporting the carbide phase was emphasised by deep-etching the samples to allow the carbides to protrude from the surface; these samples were then scratched, (100g, Vickers pyramidal diamond, Fig. 11.7a), and subjected to impact (Fig. 11.7b). The carbide particles were observed to fracture and collapse into heaps of particles (Fig. 11.7). Subsurface deformation is clear as seen from Fig. 11.8 when the scratch test was carried out using SiC fiber.

11.4 Conclusions

The abrasive wear properties of manual metal arc welded, tungsten inert gas welded and laser clad Stellite 6 hardfacing deposits have been studied and related to microstructural differences. With alumina abrasives, the wear resistance was found to increase in the order MMA→laser clad→TIG samples. The MMA samples are worst because of their coarser microstructure and lower starting hardness. The TIG samples have the highest initial wear resistance because of their higher ductility and matrix stacking fault energy. During wear, the laser clad samples were found to be the only ones to exhibit an initial increase in wear resistance, due to the relatively low stacking fault energy of the matrix phase.

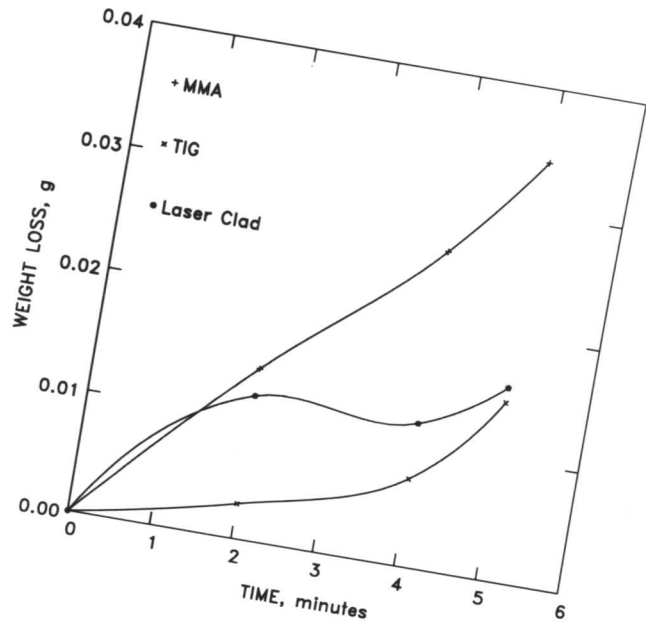
The effect of using a coarser and harder silicon carbide abrasive was to increase the wear rate in all samples; the increase is largest for the the laser and TIG samples. In fact the samples all showed very similar wear rates when tested with the silicon carbide abrasive.

This observed wear behaviour could be correlated directly with the structure of the worn surface and of the underlying regions.

Finally, it must be emphasised that the present study was deliberately conducted on samples prepared using what are believed to be *typical* process parameters. There are numerous such parameters which can be adjusted in order to alter the properties of a deposit for any single process. Indeed, it may even be the case that the chemical composition which is suited to a given process may not be good for another process. We therefore make no attempt to rank the processes in any order of excellence; such a ranking would in any case be futile since the choice of process must be highly application dependent.

11.5 References

- 1) A. P. MERCER: ' The effects of atmospheric humidity and oxygen on the wear of metals by fine abrasives ', Ph.D. Thesis, October 1985, University of Cambridge.
- 2) E. RABINOWICZ: in Proc. Conf. 'Wear of Materials 1983', 1983, ASME, New York, 12.
- 3) R. C. D. RICHARDSON: *Wear*, 1968, **11**, 245.
- 4) "Handbook of Physics and Chemistry", ed. R. C. Weast, 57 edition, CRC Press, Ohio, 1976.
- 5) T. S. EYRE: 'Wear Characteristics of Metals', Source Book on Wear Control Technology, ASM, 1978, pp.1-10.
- 6) R. W. K. HONEYCOMBE: "The Plastic Deformation of Metals", 2nd ed., 1984, Edward Arnold, London, pp.231-245.
- 7) M. A. MOORE: 'Abrasive Wear', in Proc. Conf. 'Fundamentals of Friction and Wear of Materials', 4-5 October 1980, Pittsburgh Pennsylvania, ASM.
- 8) S. W. DATE, and S. MALKIN: *Wear*, 1976, **40**, 223.
- 9) K. HOKKIRIGAWA, and K. KATO: *Tribology International*, 1988, **21**, 51.
- 10) L. E. SAMUELS: "Metallographic Polishing by Mechanical Methods", 2nd ed., 1971, Melbourne & London, pp.65-86.
- 11) J. LARSEN-BASSE: in Proc. Conf. 'Wear of Materials 1981', 1981, ASME, New York, 534.
- 12) J. LARSEN-BASSE: *Wear*, 1968, **12**, 35.
- 13) A. MISRA, and I. FINNIE: *Wear*, 1981, **65**, 359.



a

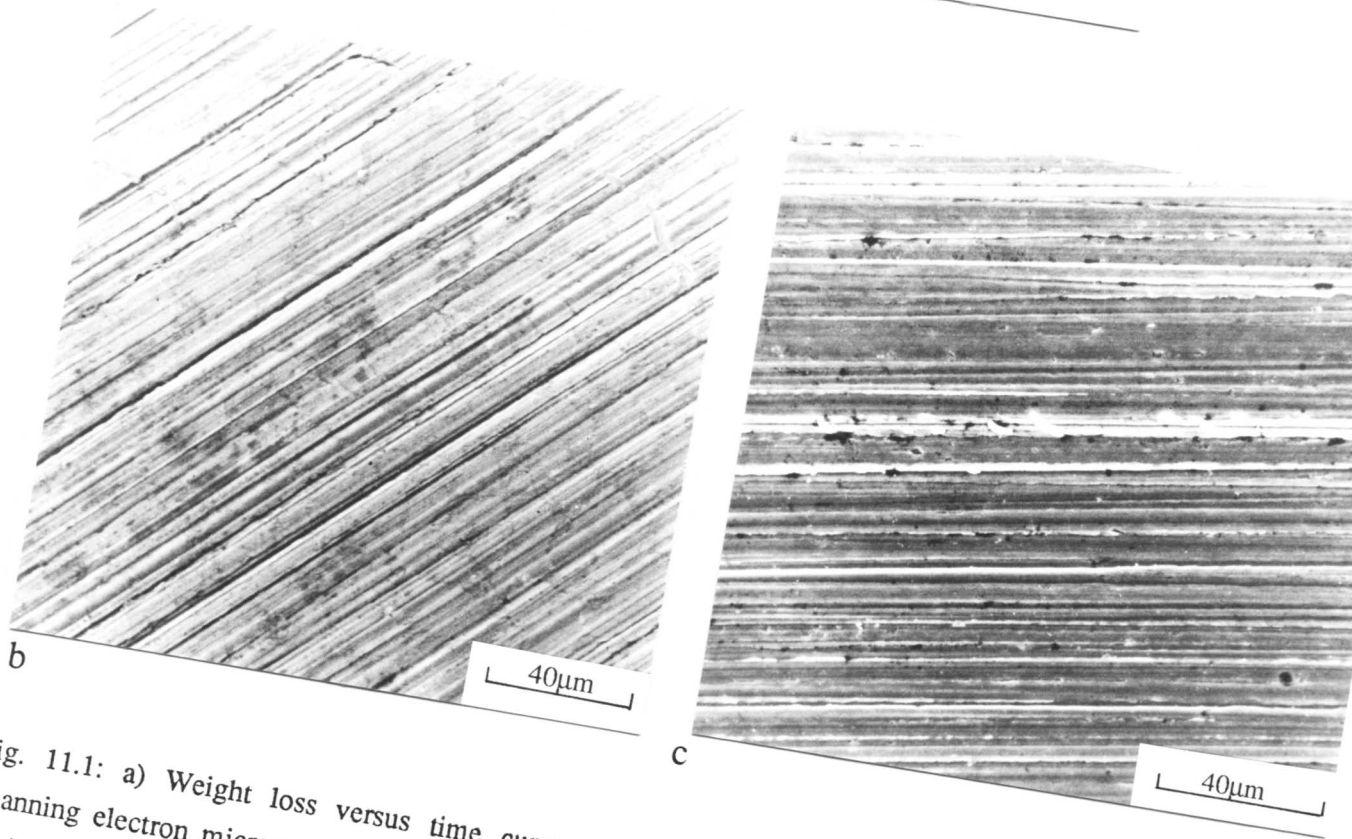
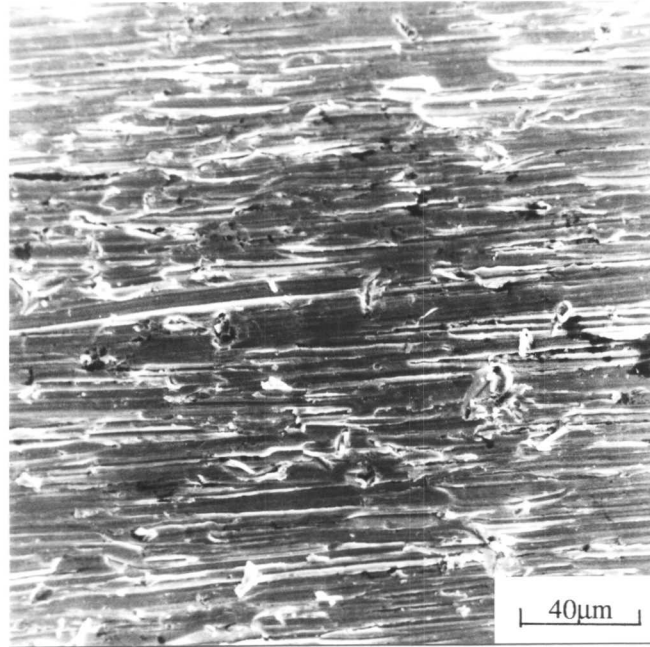
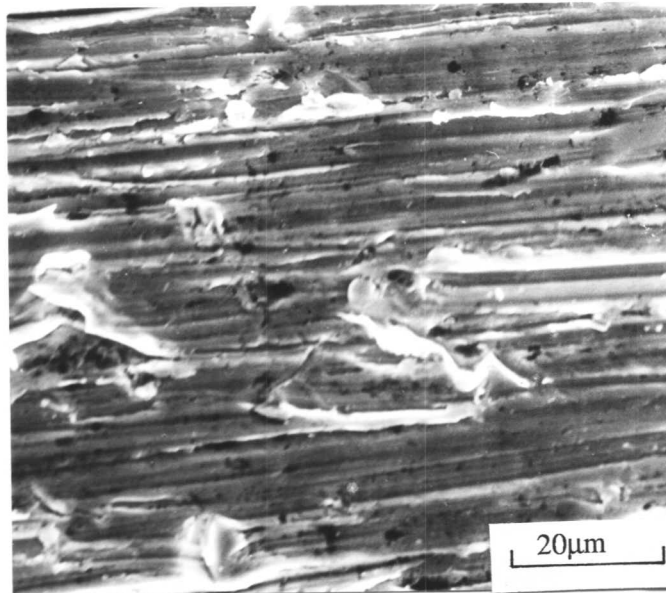


Fig. 11.1: a) Weight loss versus time curves, for wear tests done using alumina abrasive. Scanning electron micrographs of the final worn surfaces of b) MMA; c) laser clad sample and (d,e) TIG sample.

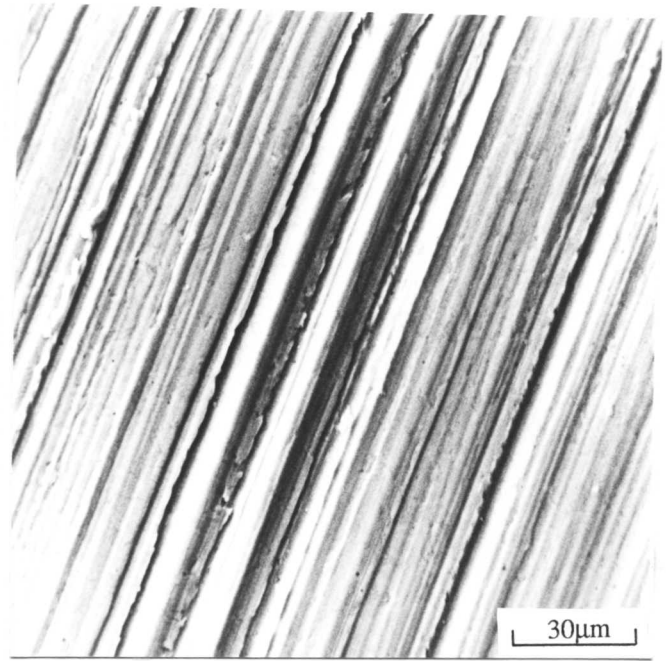
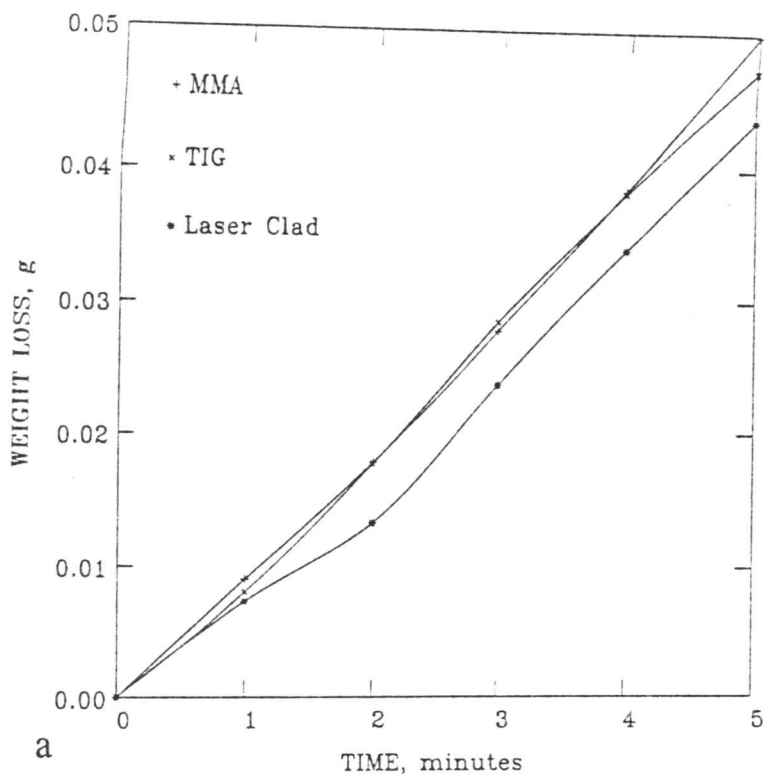


a



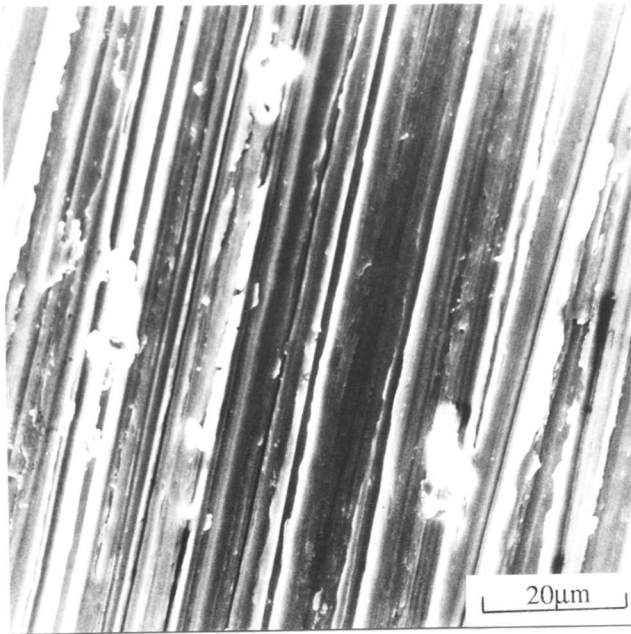
b

Fig. 11.1: a) Weight loss versus time curves, for wear tests done using alumina abrasive. Scanning electron micrographs of the final worn surfaces of b) MMA; c) laser clad sample and (d,e) TIG sample.

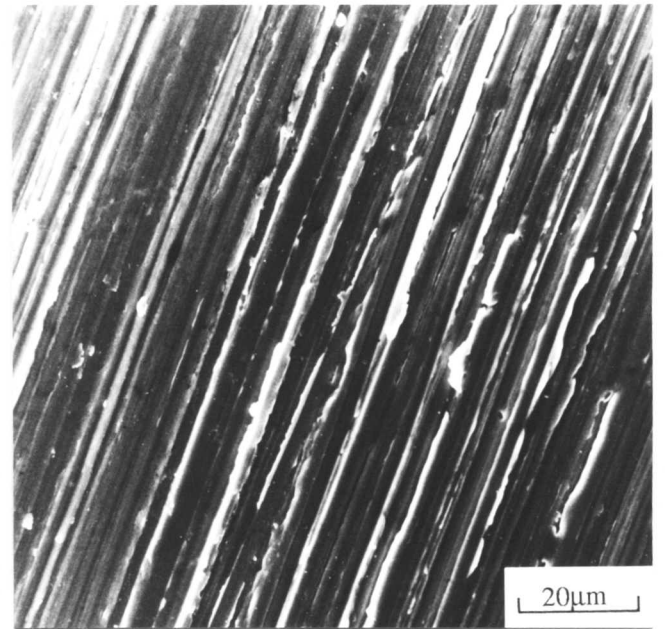


a

b

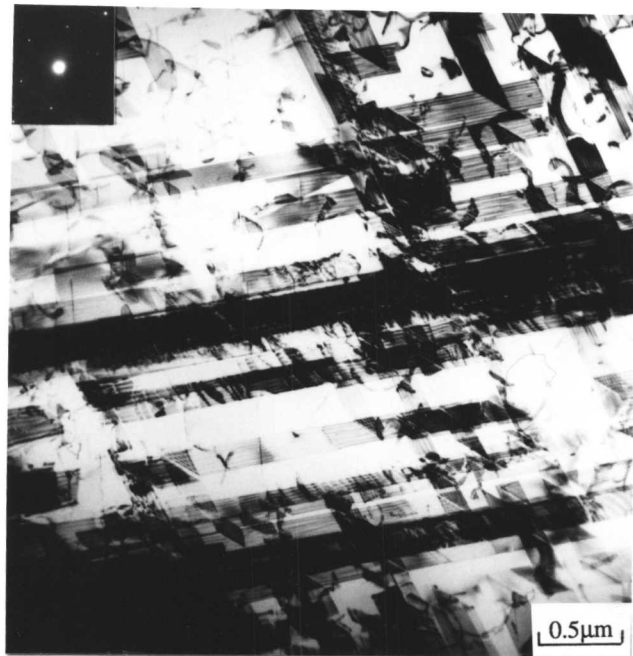


c

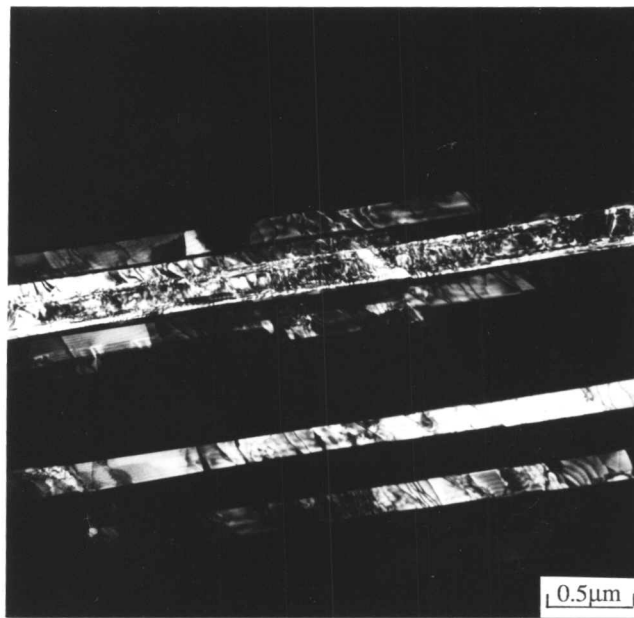


d

Fig. 11.2: a) Weight loss versus time curves, for wear tests done using silicon carbide abrasive; (b-d) scanning electron micrographs of the final worn surfaces of MMA, TIG and laser clad samples.



a



b

Fig. 11.3: Transmission electron micrographs from an abraded MMA sample: a) bright field image and electron diffraction pattern confirming the presence of hcp platelets ($[0\ 0\ 0\ 1]$ zone axis); b) dark field image of hcp platelets.

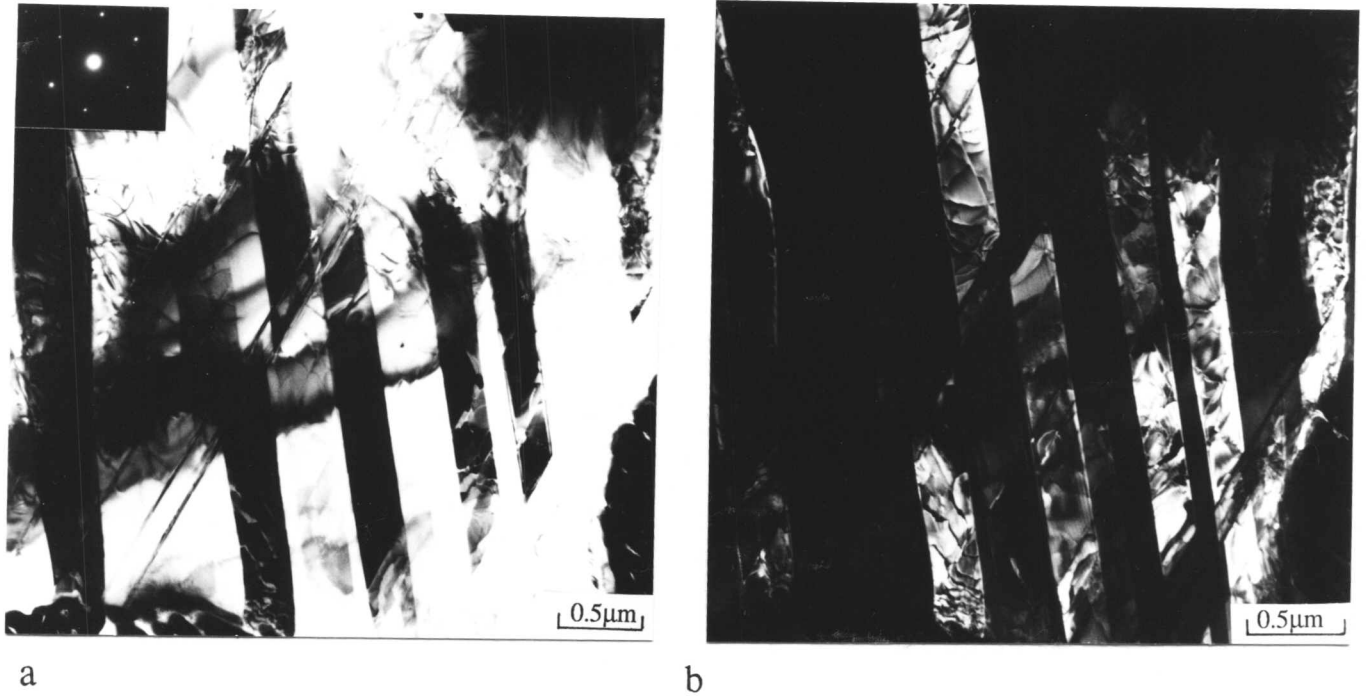


Fig. 11.4: Transmission electron micrographs from an abraded Laser clad sample; a) bright field image and electron diffraction pattern confirming the presence of hcp platelets ($[1 \bar{2} 1 \bar{3}]$ zone axis); b) dark field image of hcp platelets.

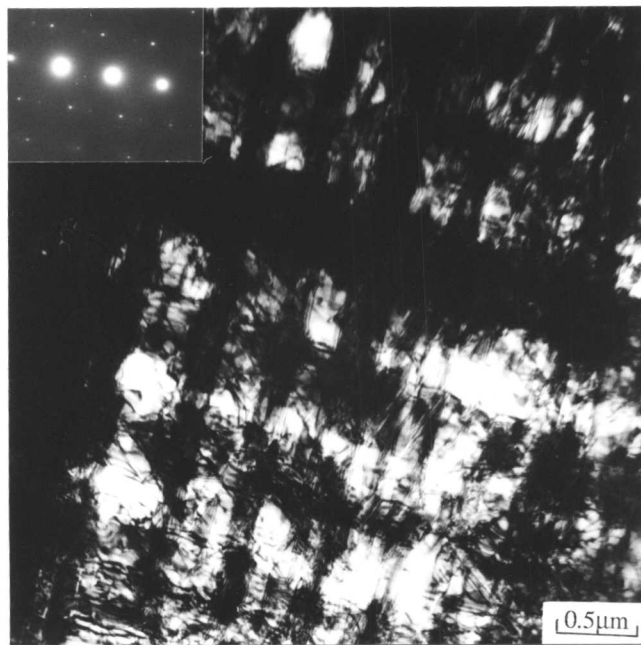
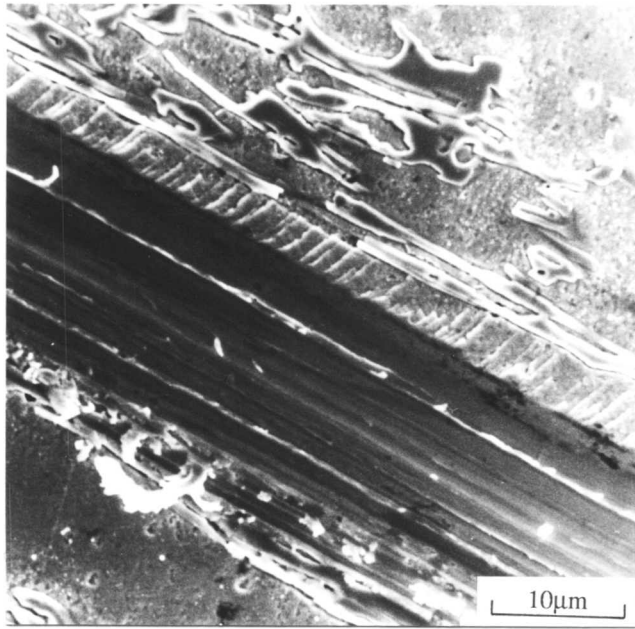
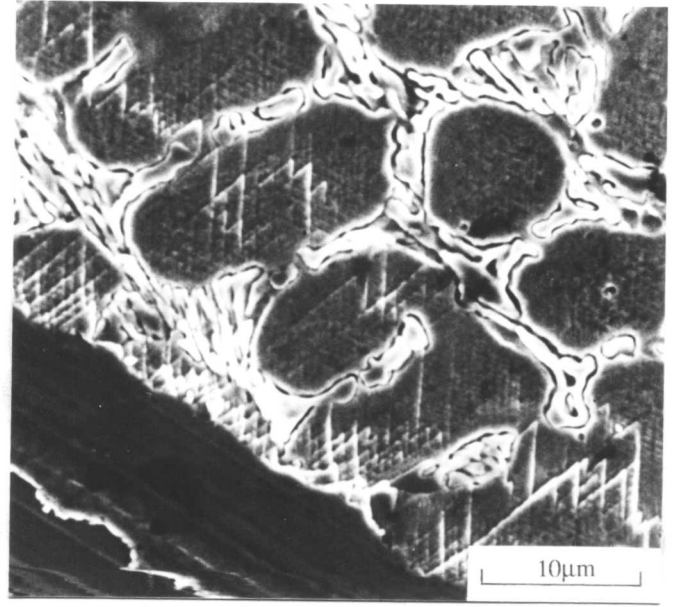


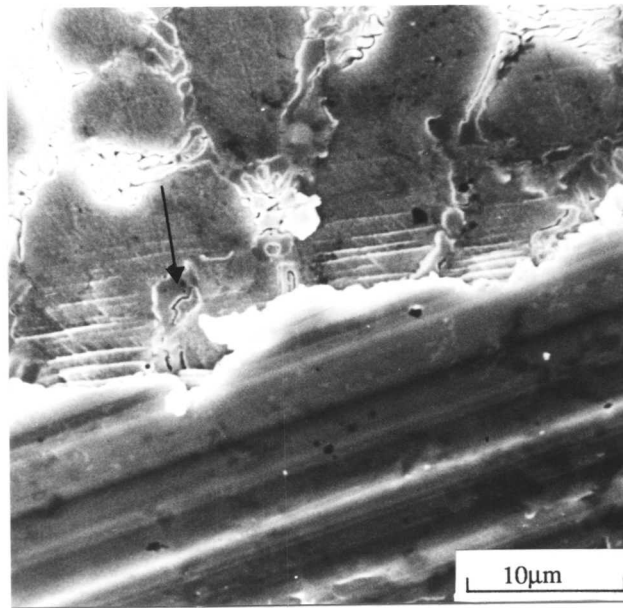
Fig. 11.5: Transmission electron micrograph from an abraded TIG specimen.



a



b



c

Fig. 11.6: Scanning electron micrographs from scratched specimens: a) MMA 100g; b) MMA 500g; c) MMA 1000g (arrow indicates the matrix cracking); d) TIG 500g; e) laser clad 500g.

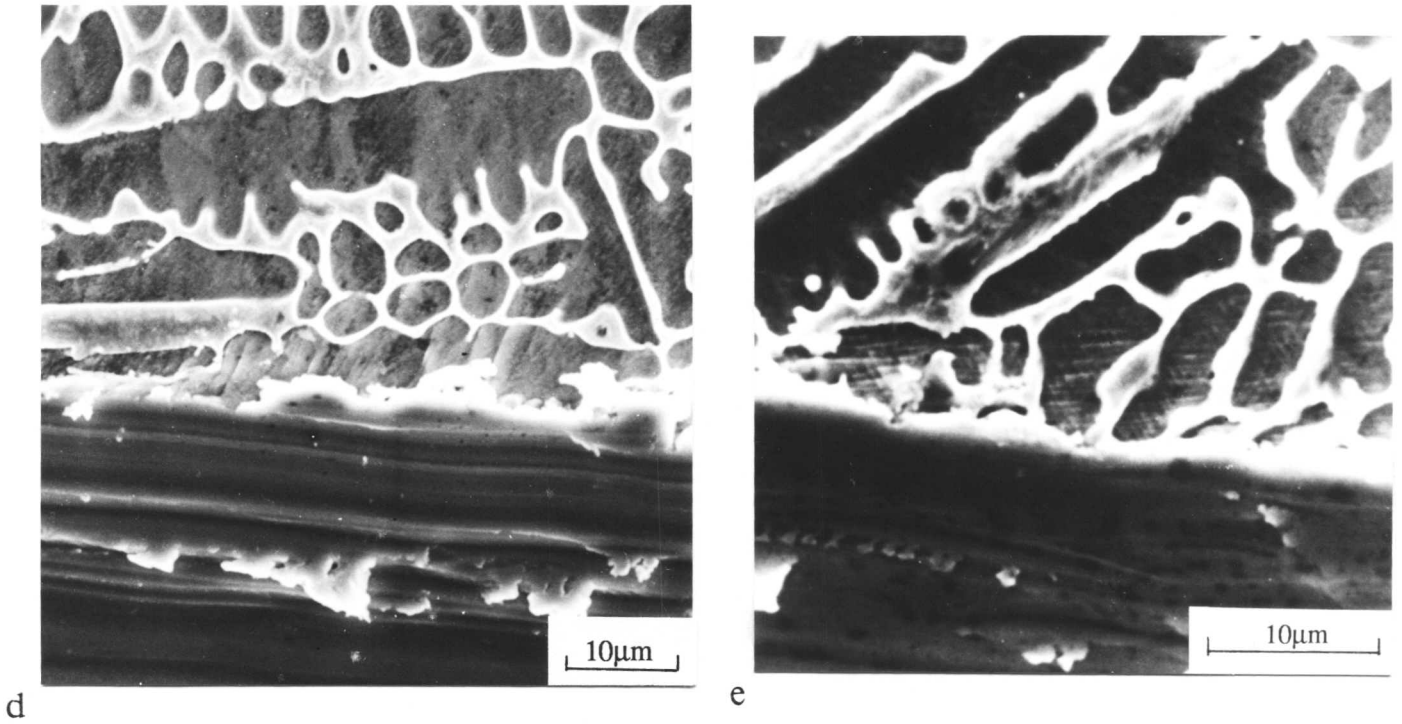


Fig. 11.6: Scanning electron micrographs from scratched specimens: a) MMA 100g; b) MMA 500g; c) MMA 1000g (arrow indicates the matrix cracking); d) TIG 500g; e) laser clad 500g.

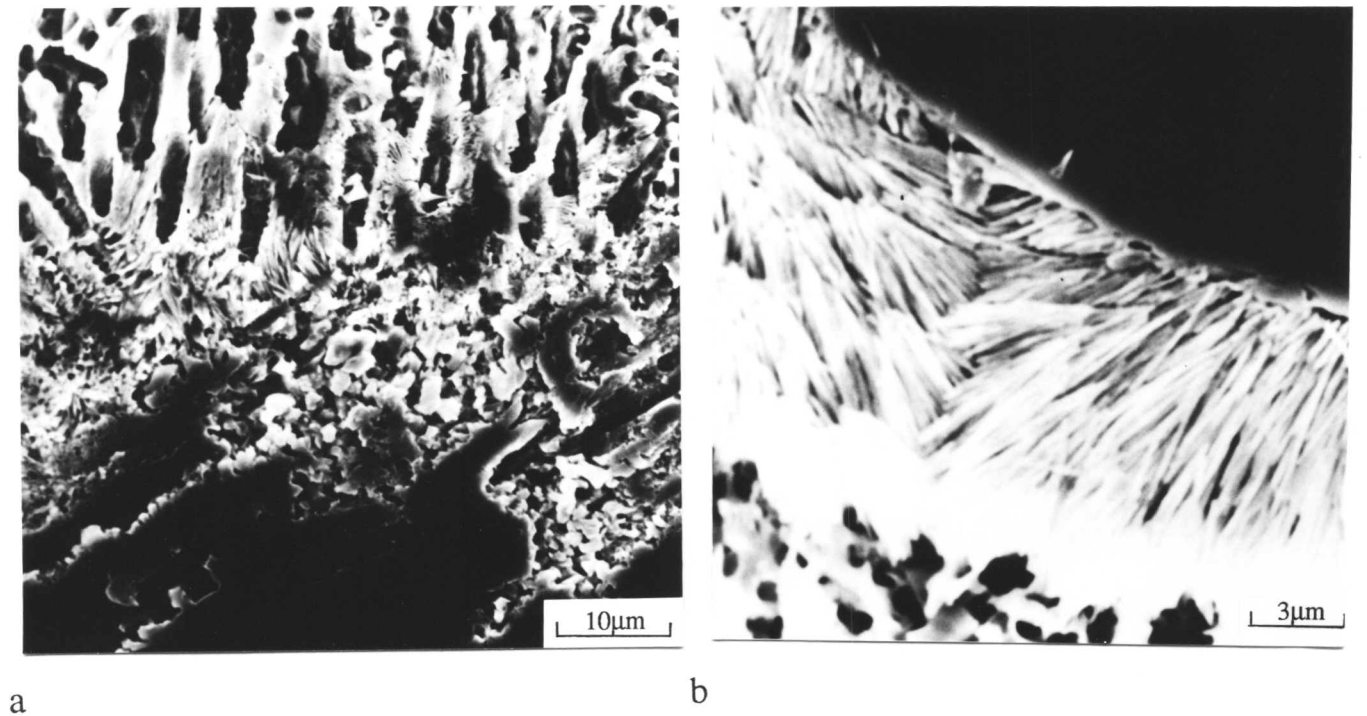


Fig. 11.7: Scanning electron micrographs from a deep-etched specimen which was subsequently a) scratched with a Vickers diamond; b) subjected to impact, illustrating the collapse of the unsupported eutectic carbides.

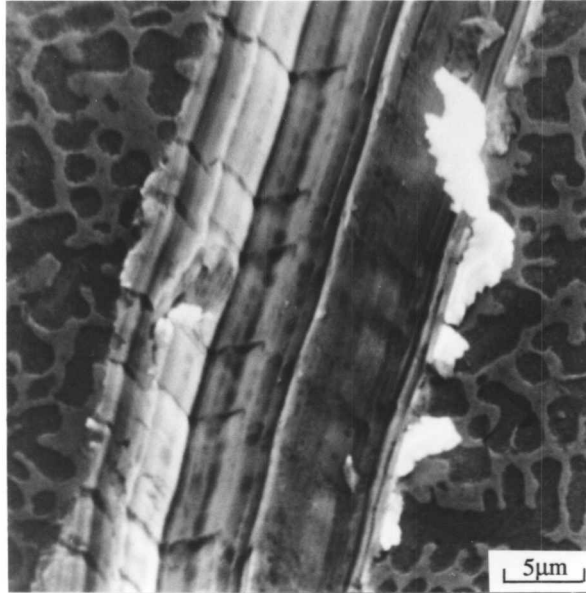


Fig. 11.8: Scanning electron micrograph from scratched specimen with 100g using SiC fiber (100μm), illustrating the subsurface deformation.